

AD-A044 436

WASHINGTON UNIV SEATTLE DEPT OF CHEMISTRY  
PROBLEMS OF DIFFUSION IN A LOW PRESSURE GAS STREAM AS RELATED T--ETC(U)  
SEP 77 D G KEIL, J F BURKHALTER  
NR092-549-TR06

F/G 7/4

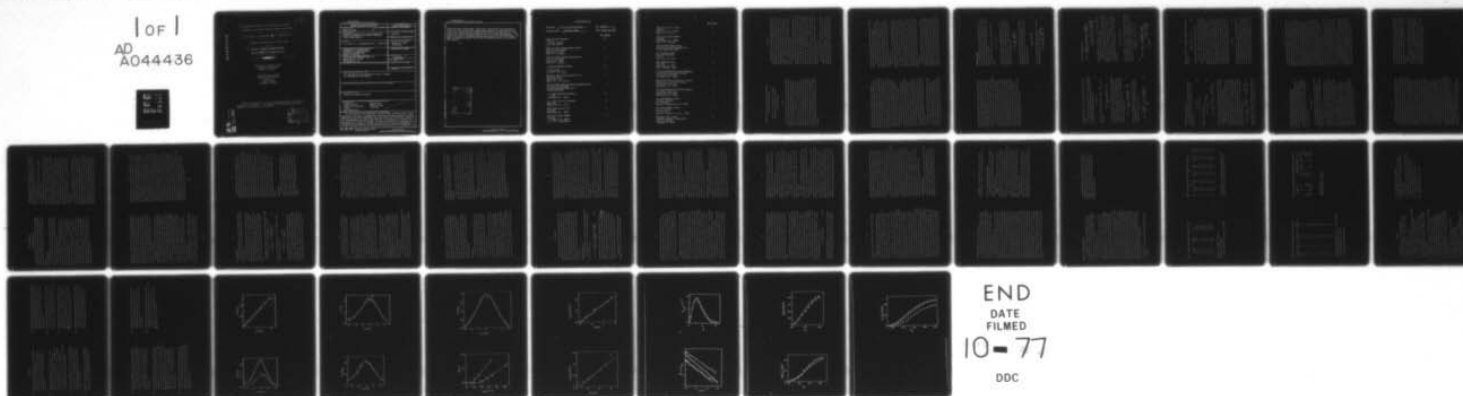
N00014-75-C-0690

NL

UNCLASSIFIED

1 OF 1  
AD  
A044436

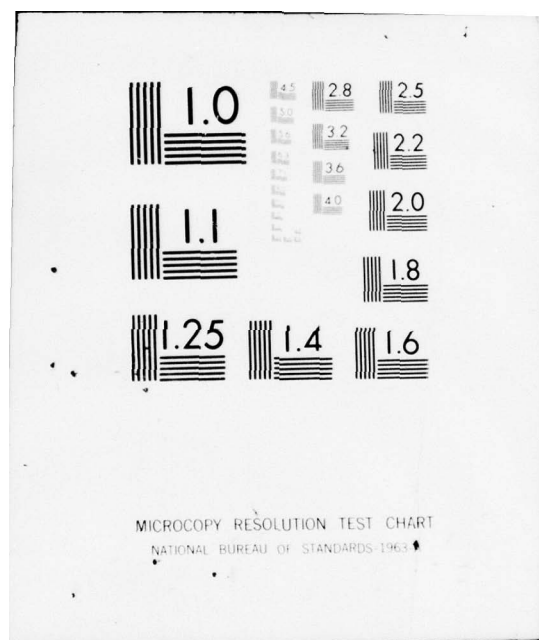
SEP 77



END  
DATE  
FILMED

10-77

DDC



AD A 044436

6

Problems of Diffusion in a Low Pressure Gas Stream  
as Related to the Polanyi Diffusion Flame (Cloud) Method.

12

10

D. G. Keil, J. F. Burkhalter and B. S. Rabinovitch

Prepared for publication in J. Phys. Chem.

9

Technical Report No. NR092-549-TR06

14

Contract N00014-75-C-0690, NR092-549

15

11

2 Sept 1977

12 61 p.

Department of Chemistry, BG-10  
University of Washington  
Seattle, WA 98195

OFFICE OF NAVAL RESEARCH  
Department of the Navy  
Code 473  
800 N. Quincy  
Arlington, VA 22217

Reproduction in whole or in part is permitted for any purpose of the  
United States Government. This document has been approved for public  
release; its distribution is unlimited.

AD No. \_\_\_\_\_  
DDC FILE COPY

DDC  
RECORDED  
SEP 22 1977  
B

370 274

cut

Unclassified

SECURITY CLASSIFICATION OF THIS PAGE (When Data Entered)

REPORT DOCUMENTATION PAGE		READ INSTRUCTIONS BEFORE COMPLETING FORM
1. REPORT NUMBER NR092-549-TR06	2. GOVT ACCESSION NO.	3. RECIPIENT'S CATALOG NUMBER
4. TITLE (and Subtitle) Problems of Diffusion in a Low Pressure Gas Stream as Related to the Polanyi Diffusion Flame (Cloud) Method		5. TYPE OF REPORT & PERIOD COVERED Technical
7. AUTHOR(s) D. G. Keil, J. F. Burkhalter and B. S. Rabinovitch		6. PERFORMING ORG. REPORT NUMBER
9. PERFORMING ORGANIZATION NAME AND ADDRESS Professor B. S. Rabinovitch Department of Chemistry BG-10 University of Washington Seattle, WA 98195		8. CONTRACT OR GRANT NUMBER(s) N00014-75-C-0690 NR 092-549
11. CONTROLLING OFFICE NAME AND ADDRESS Office of Naval Research, Code 473 Department of the Navy 800 N. Quincy Arlington, VA 22217		10. PROGRAM ELEMENT, PROJECT, TASK AREA & WORK UNIT NUMBERS
14. MONITORING AGENCY NAME & ADDRESS (if different from Controlling Office)		12. REPORT DATE 1 September 77
		13. NUMBER OF PAGES 59
		15. SECURITY CLASS. (of this report)
		15a. DECLASSIFICATION/DOWNGRADING SCHEDULE
16. DISTRIBUTION STATEMENT (of this Report) This document has been approved for public release; its distribution is unlimited.		
17. DISTRIBUTION STATEMENT (of the abstract entered in Block 20, if different from Report)		
18. SUPPLEMENTARY NOTES Submitted to Chemical Reviews		
19. KEY WORDS (Continue on reverse side if necessary and identify by block number) Diffusion Energy Transfer Equation of Continuity Flames High Temperature Steady-state Thermal Systems Transients APPROXIMATELY EQUAL TO		
20. ABSTRACT (Continue on reverse side if necessary and identify by block number) In anticipation of the application of the Polanyi diffusion flame (cloud) technique to the study of unimolecular reactions and energy transfer at higher temperatures, we have investigated some experimental and theoretical aspects of the time-dependent and steady-state behavior of diffusion of a reactant into a low pressure (~1 torr) gas stream. A study of the diffusion of Hg vapor in N <sub>2</sub> atmospheric gas was made. The effects of the Hg inlet nozzle configuration and the inlet gas flow rate on the diffusion process and on the atmospheric gas		

DD FORM 1 JAN 73 1473

EDITION OF 1 NOV 65 IS OBSOLETE  
S/N 0102-LF 014-6601

Unclassified

SECURITY CLASSIFICATION OF THIS PAGE (When Data Entered)

Unclassified

SECURITY CLASSIFICATION OF THIS PAGE(When Data Entered)

stream have been investigated. Monte Carlo calculations have been made to reveal the time-dependent and steady-state behavior of a species diffusing from a point source into gas streams having various velocity profiles. Some aspects of a reactive diffusing species are also treated mathematically. The present results are integrated with previous results of other investigators in order to provide an overall view of the relationship between real and model flow systems.

ACCESSION for	
NTIS	White Section <input checked="" type="checkbox"/>
DDC	Buff Section <input type="checkbox"/>
UNCLASSIFIED	<input type="checkbox"/>
BY	
DISTRIBUTION CODES	
SPECIAL	
A	

Unclassified

SECURITY CLASSIFICATION OF THIS PAGE(When Data Entered)

DISTRIBUTION LIST

Contractor University of Washington

NR 092-549

Contract Number N00014-75-C-0690

Date August 15, 1977

No. Copies

Office of Naval Research Code 473 Arlington, VA 22217 Attn: Dr. Miller	10
Office of Naval Research Branch Office 1030 East Green Street Pasadena, CA 91106 Attn: Dr. R. Marcus	1
Office of Naval Research Branch Office 535 S. Clark Street Chicago, IL 60605 Attn: Dr. J. Smith	1
Defense Documentation Center Bldg. 5 Cameron Station Alexandria, VA 22314	12
Office of Naval Research Branch Office 495 Summer Street Boston, MA 02210 Attn: Dr. L. H. Peebles	1
Office of Naval Research Resident Representative University of Washington 3710 Brooklyn Avenue NE, Unit 2 Seattle, WA 98195	1
U. S. Naval Research Laboratory Code 2627 Washington, D.C. 20375	6
U. S. Naval Research Laboratory Code 2629 Washington, D.C. 20375	6
Naval Research Laboratory Code 6100 Washington, D.C. 20375	1
Naval Air Systems Command Code 440 Washington, D.C. 20360 Attn: Dr. H. Rosenwasser	1

	<u>No. Copies</u>
Naval Sea Systems Command SEA-0331 Washington, D.C. 20362 Attn: Mr. J. Murrin	1
Naval Sea Systems Command SEA-0332 Washington, D.C. 20362 Attn: Dr. A. Amster	1
Naval Surface Weapons Center Research and Technology Dept.-WR Silver Spring, MD 20910	1
Naval Weapons Center Research Department Code 60 China Lake, CA 93555	1
Naval Weapons Center Code 608 China Lake, CA 93555 Attn: Ronald L. Derr	3
Air Force Office of Scientific Research Directorate of Aerospace Sciences Bolling Air Force Base Washington, D.C. 20332	1
Air Force Office of Scientific Research Directorate of Chemical Sciences Bolling Air Force Base Washington, D.C. 20332	1
Air Force Office of Scientific Research Directorate of Physics Bolling Air Force Base Washington, D.C. 20332	1
U.S. Army Research Office Chemistry Division P.O. Box 12211 Research Triangle Park, N.C. 27709	1
U.S. Army Research Office Physics Division P.O. Box 12211 Research Triangle Park, N.C. 27709	1
Professor S.N.B. Murthy Technical Director, Project SQID Purdue University Lafayette, IN 47907	5

Problems of Diffusion in a Low Pressure Gas Stream as Related to  
the Polanyi Diffusion Flame Method

by D. G. Keil, J. F. Burkhalter and B. S. Rabinovitch  
Department of Chemistry, University of Washington  
Seattle, Washington 98195

Abstract

In anticipation of the application of the Polanyi diffusion flame (cloud) technique to the study of unimolecular reactions and energy transfer at higher temperatures, we have investigated some experimental and theoretical aspects of the time-dependent and steady-state behavior of diffusion of a reactant into a low pressure ( $\sim 1$  torr) gas stream. A study of the diffusion of Hg vapor in  $N_2$  atmospheric gas was made. The effects of the Hg inlet nozzle configuration and the inlet gas flow rate on the diffusion process and on the atmospheric gas stream have been investigated. Monte Carlo calculations have been made to reveal the time-dependent and steady-state behavior of a species diffusing from a point source into gas streams having various velocity profiles. Some aspects of a reactive diffusing species are also treated mathematically. The present results are integrated with previous results of other investigators in order to provide an overall view of the relationship between real and model flow systems.

Introduction

The original diffusion flame technique pioneered by Hartel and Polanyi<sup>1,2</sup> provided a method for the study of fast bimolecular reactions under pseudo-first order conditions. The flow velocity of the atmospheric reactant was usually much less than the diffusional velocity of the nozzle reactant. The diffusion of the nozzle gas provided a time reference by which reaction rates could be determined. The diffusion "cloud" technique, as it has been termed by later workers<sup>3</sup> is, in general, characterized by the use of a "point" source of substrate in a flowing atmospheric reactant under conditions such that heterogeneous reactant collisions are negligible.

In early use of the technique, systematic deviations between experimental results and predictions from a simple model of spherical diffusion were noted.<sup>2</sup> Heller<sup>4</sup> proposed restrictions on the allowed ratio of the reactant nozzle velocity to the diffusion coefficient in the atmospheric gas, for obedience to the simple model. Garvin, Guinn and Kistiakowsky<sup>5</sup> found that this ratio can increase with decrease in nozzle radius. Reed and Rabinovitch<sup>6</sup> generalized Heller's criteria for various nozzle radii. They also solved the equation for diffusion and first order reaction from a point reactant source in a flowing medium having constant velocity. Recently, Mintz and LeRoy<sup>7</sup> clarified Heller's criteria. The last ten years has seen several experimental applications of the method<sup>8-10</sup> to the determination of bimolecular reaction rates.

No application of the diffusion cloud technique to the study of unimolecular reactions appears to have been made. It is an attractive technique for such studies, particularly at high temperatures. Such an application introduces new experimental features. Moreover, some hydrodynamic and experimental aspects of the existing technique remain unclear. Before undertaking to apply a diffusion

cloud technique to the study of unimolecular reactions, we considered it desirable to examine the existing theoretical treatments of the diffusion-flow equations and to reconcile some apparent discrepancies, as well as to investigate, experimentally, some important and uncertain aspects of experimental design. Thus, the introduction of a large atmospheric flow effectively expands the reaction time scale in the flow direction. This flow must be included in the continuity equation and be defined in terms of an appropriate velocity field; the mathematical treatment of the experimental data is crucial to its interpretation. It appears useful, in the remainder of this section, to provide a brief qualitative summary of recent experimental work and approaches to the treatment of diffusion and bimolecular reaction from a point source in a flowing gas. Mathematical aspects will be summarized in the following section.

Walker and Westenberg<sup>11</sup> used a "point" source to measure diffusion coefficients in a cylindrical flow tube in which a radially-independent atmospheric velocity field ("flat" profile) was artificially produced. They investigated the perturbations of the atmospheric velocity field at high pressure (0.1 atm) caused by flow from an axial nozzle. The nozzle flow rate which caused the least perturbation corresponds approximately (as inferred from their paper) to the values predicted by Heller's criteria as modified by the later work.<sup>6,7</sup> Since these experiments involved the problem of matching of nozzle and atmospheric flows in the presence of a stagnant boundary layer on the nozzle, the seemingly equivalent requirements for static and flowing atmospheric gases may be accidental.

The suggestion by Snow and Westenberg<sup>12</sup> that the technique of a point source in a "flat" atmospheric velocity field could be used in the study of fast pseudo-first order reactions was followed by Frazier and Kooyman.<sup>13</sup> Their results showed the need to correct for a deficit of the dilute atmospheric reactant in the region near the nozzle, under their conditions. They neglected the effect of the nozzle reactant flow which also must be examined if the region

near the nozzle is of experimental interest. Moreover, the nozzle configuration also affects the adjacent velocity field and must be considered.

In their diffusion flame investigation of the reactions of phosphorous vapor in oxygen, Nevrovskii and Soroka<sup>10</sup> observed a marked change in the flame shape when the nozzle reactant carrier gas was switched from He to Ar at the same volume flow rates. They suggested that the observed behavior is a consequence of momentum as well as diffusion effects. They did not elaborate on the relative magnitudes of these effects nor did they consider the importance of atmospheric gas flow.

A "point" source on the axis of a tube with fully developed laminar flow (parabolic velocity profile) has been used by Talhoze et al.<sup>8</sup> in the measurement of pseudo-first order and consecutive pseudo-first order bimolecular reaction rates. However, in the treatment of the results<sup>3</sup> they approximated the effective velocity field as a flat field with a velocity equal to the laminar maximum (tube axis) velocity; they derived criteria for conditions of high flow velocities so as to limit excursion of the reactants into regions of low velocities. Later time-dependent calculations on an initial plane sheet of ions in a parabolic flow profile<sup>14</sup> suggest that the effective axial velocity may lie between the maximum and average flow velocities when significant radial diffusion has taken place. However, this proposition has not yet been actually tested for a point source.

The solution of the equation for diffusion from a point source in laminar flow was approximated by Brown<sup>15</sup> with use of a relaxation technique. To avoid steep gradients near the source, an artificially large source region was incorporated into the calculation. More recently, Nevrovskii<sup>16</sup> has approximated the steady-state solution for diffusion and first order reaction for a point source in a cylindrical tube with laminar flow. He used an expansion in hypergeometric functions. Due to the truncated expansion of the source delta function, the source region is large in the radial plane. The technique can be extended to the case

of no reaction and additional terms can be included to reduce the source size. Nevrovskii has considered a limited number of reactive cases which cannot be directly compared to Brown's calculation derived for pure diffusion. However, the calculations do indicate that the criteria of Tal'roze and co-workers are useful under many experimental conditions. Unfortunately, there is no known information on the region near the source and no experimental evidence for the region of validity of the above calculations. Nozzle drag has not been considered.

We have constructed a Hg diffusion test apparatus in order to study the flow conditions near a real point source. We have investigated the nature of the actual velocity profile to confirm the presence of laminar flow. Perturbations of the flow (i.e., by the nozzle) have also been investigated. Nozzles of several sizes, shapes and flow orientation have been used. Both transient and steady state measurements have been made for Hg vapor diffusing into a  $N_2$  stream. Comparisons have been made with theory and with the computer simulated time development of diffusion from a point source in various flow profiles. Evidence for perturbation of the flow field by the reactant gas source is examined. We also show how a transient region (non-equilibrium reaction rate) can be considered in the solution of the diffusion equation.

### Mathematical Treatment

The mathematical description of the concentration distribution for a reactant which diffuses from a point source into a medium moving with constant velocity, and in which the diffusing material undergoes first-order reaction, has been derived in basically two ways. Both methods find origins in Wilson's treatments of heat conduction.<sup>17</sup>

One approach is to find a solution for the steady state continuity equation,

$$D \nabla^2 C - kC - U \frac{\partial C}{\partial z} = 0 \quad I$$

where  $D$  represents a concentration independent diffusion coefficient of the reactant (concentration  $C$ ) in the medium which flows in the  $z$  direction at velocity  $U$ ;  $k$  is the first order reaction rate constant. Equation I was solved by Wilson<sup>17</sup> for the case  $k = 0$ . Reed and Rabinovitch<sup>5</sup> extended the solution to finite  $k$  and obtained the form

$$C(z, R) = \frac{A}{R} \exp \left( \frac{Uz}{2D} - R \sqrt{\frac{U^2}{4D^2} + \frac{k}{D}} \right) \quad II$$

where  $R$  is the radial distance from the source and  $A$  is a constant which is found by the application of an appropriate boundary condition. In the limit of small  $R$  (and  $z$ ), eq. II reduces to  $C = A/R$  to which a point source boundary condition may be applied:

$$I = \lim_{R \rightarrow 0} \left( -D \frac{\partial C}{\partial R} 4\pi R^2 \right) \quad III$$

where  $I$  is the intensity of the source (particles/time). This leads to the well-known result (which simplifies for the case  $k = 0$ ),

$$C(z, R) = \frac{I}{4\pi DR} \exp \left( \frac{Uz}{2D} - R \sqrt{\frac{U^2}{4D^2} + \frac{k}{D}} \right) \quad IV$$

Boundary conditions other than eq. III may be applied to eq. II, e.g., see ref. 6.

The second approach used by Tal'roze et al.<sup>3</sup> is based on an instantaneous pulse point source (a description attributed by Wilson to Lord Kelvin). The time dependent continuity equation in the case  $U = 0$

$$D\nabla^2 C - kC = \frac{\partial C}{\partial t} \quad V$$

which, for an instantaneous point source of intensity  $I$  at  $R = t = 0$ , has the solution

$$C(R, t) = \frac{I dt}{(4\pi Dt)^{3/2}} \exp \left[ -\frac{R^2}{4Dt} - kt \right] \quad VI$$

A continuous point source is simply treated as a collection of instantaneous pulses of different ages. The concentration distribution for each pulse is spherically symmetric. In order to introduce an atmospheric velocity, one requires that the center of mass of a particular instantaneous pulse be located at  $z = Ut$ , where  $t$  is the "age" of the pulse. A continuous source in a flow is then described by eq. VII.

$$C(z, \rho, s) = \int_0^s \frac{I}{(4\pi Dt)^{3/2}} \exp \left[ -\frac{(z-Ut)^2 + \rho^2}{4Dt} - kt \right] dt \quad VII$$

where  $C(z, \rho, s)$  represents the concentration at time  $s$  at a point with cylindrical coordinate  $z$  and  $\rho$ . On rearranging terms in the exponential and substituting  $\xi = \frac{R}{2\sqrt{Dt}}$  ( $R^2 = z^2 + \rho^2$ ),

$$C(z, R, s) = \frac{I \exp(\frac{Uz}{2D})}{2\pi^{3/2} D^{3/2}} \int_0^s \frac{\exp \left[ -\xi^2 - \frac{R^2(U^2 + 4Dk)}{16 D^2 \xi^2} \right]}{2\sqrt{Ds}} d\xi \quad VIII$$

This can be integrated<sup>18</sup> to give

$$C(z, R, s) = \frac{I \exp(\frac{Uz}{2D})}{8\pi D R} \left\{ \exp \left( \frac{R}{2D} \sqrt{U^2 + 4Dk} \right) \left[ 1 - \operatorname{erf} \left( \frac{R + s \sqrt{U^2 + 4Dk}}{2\sqrt{Ds}} \right) \right] + \exp \left( -\frac{R}{2D} \sqrt{U^2 + 4Dk} \right) \left[ 1 - \operatorname{erf} \left( \frac{R - s \sqrt{U^2 + 4Dk}}{2\sqrt{Ds}} \right) \right] \right\} \quad IX$$

which in steady state ( $s \rightarrow \infty$ ) yields eq. II. The instantaneous point source method readily leads to the time-dependent solution.

We now wish to show that eq. IX can also be found in a somewhat different way in order to allow the treatment of more complex rate behavior (i.e., time-dependent variation of  $k$  for a non-steady state system). We start with the non-reactive diffusion case, i.e.,  $D\nabla^2 = \frac{\partial C}{\partial t}$  and proceed as above. The result is the same as eq. IX with  $k = 0$ . The reaction process is introduced by integrating over  $s$  with weighting appropriate to a first order reaction rate. Hence,

$$C^r(z, R, s) = \int_0^\infty C^0(z, R, s) \eta_s ds \quad X$$

where the superscripts  $r, 0$  signify concentrations calculated for the reactive and the non-reactive case, respectively. The weighting factor  $\eta_s$  represents the fraction of reactant molecules from an instantaneous source that react in the time interval  $s$  to  $s+ds$  according to a first order rate law,

$$\eta_s = \frac{d(C_s/C_0)}{ds} \bigg|_s = k e^{-ks}; \int_0^\infty k e^{-ks} ds = 1 \quad XI$$

Thus

$$C^r(z, R, s) = \int_0^\infty \frac{k e^{-ks}}{8\pi D R} \exp \left( \frac{Uz}{2D} \right) \left\{ \exp \left( \frac{R}{2D} \right) \left[ 1 - \operatorname{erf} \left( \frac{R+Us}{2\sqrt{Ds}} \right) \right] + \exp \left( -\frac{R}{2D} \right) \left[ 1 - \operatorname{erf} \left( \frac{R-Us}{2\sqrt{Ds}} \right) \right] \right\} ds \quad XII$$

$$\equiv \int_0^\infty k e^{-ks} C^0 ds$$

Evaluation of the integral gives eq IX.

In a similar way, a transient region for reaction can be introduced into the description of a system. In the simple case,  $k=0$  for  $0 \leq s \leq s_0$ , and  $k=k$  for  $s \geq s_0$ .

$$\begin{aligned} \eta_s &= 0, \quad 0 \leq s \leq s_0 \\ \eta_s &= ke^{-k(s-s_0)}, \quad s \geq s_0. \end{aligned} \quad \text{XIII}$$

Comparison with eq. XIII shows that

$$C''(z, R, s) = \int_{s_0}^{\infty} ke^{-k(s-s_0)} C_0(s) ds. \quad \text{XIV}$$

$$\text{or} \quad C''(z, R, s) = \int_0^{\infty} ke^{-k(s-s_0)} C_0(s) ds - \int_0^{s_0} ke^{-k(s-s_0)} C_0(s) ds$$

The first term is simply eq. IX times an additional factor  $e^{-ks_0}$ ; the second term can be integrated by parts but need not be presented here. More complicated reaction models require numerical integration techniques.

Another application of the instantaneous point source method of calculation is to the derivation of product distributions. Tal'roze<sup>3</sup> used the following method to find the distribution of a product which itself undergoes first-order reaction. Each point in space is considered a source of product with intensity  $I' = knC''(z, R)$ , where  $n$  is the ratio of product to reactant molecules for a reactive event (rate constant  $k$ ) and  $C''(z, R)$  is given by eq. IV. The steady state contribution of a source at  $(z_1, \bar{R}_1)$  to the concentration of product  $P$  at any other point  $(z_1, \bar{R}_1)$  is

$$C^P(z_1, \bar{R}_1) = \frac{I'}{4\pi D'(\bar{R}_1 - \bar{R}_1)} \exp \left[ \frac{U(z_1 - z_1')}{2D'} - (\bar{R}_1 - \bar{R}_1') \sqrt{\frac{U^2}{4D'^2} + \frac{k'}{D'}} \right] \quad \text{XV}$$

where  $\bar{R}_n$  is the position vector of the appropriate point, and the primes refer to the product species. In the case  $P$  is a stable species ( $k' = 0$ ) and has the

same diffusion coefficient as the reactant, conservation of material leads directly to,

$$C^P(z, R, s) = C^O(z, R, s) - C(z, R) \quad \text{XVI}$$

This case would apply for a unimolecular isomerization reaction.

In principle, the method described above for non-steady state transient behavior can also be extended to the spatial distribution of reaction products.

Consider next the case of variable atmospheric flow velocity. Existing treatments are less certain. In fact, Tal'roze et al<sup>3</sup> approximated their reaction rate data for a point source in a laminar parabolic flow with an equation of the form of eq. II, where  $U$  was taken as twice the average atmospheric flow velocity. They proposed that this is adequate as long as axial concentration measurements are made and the atmospheric velocity to diffusion coefficient ratio is sufficiently high so that for the average path length, the maximum excursion from the axis with return to the measurement point for the nozzle reactant is much less than the distance from the axis at which the atmospheric velocity departs significantly from the axial velocity. Thus, if a 10% velocity deviation were tolerable, for laminar flow the criterion is

$$\frac{U}{D} \gg \frac{40z}{\pi R_0^2} \quad \text{XVII}$$

where  $R_0$  is the radius of the tube. If valid, this would reduce the need for a solution to the continuity equation in laminar flow (eq. I, with  $U = U_0[1 - (R/R_0)^2]$ ). Nevrovskii<sup>16</sup> has investigated particular series solutions for this more complicated case for several sets of conditions ( $k, D, U$  and  $R_0$ ). His findings relative to the above criterion will be considered in the results section. However, his results cannot readily be extended to the non-reactive case as can the closed analytical solution described previously. The relaxation

calculations of Brown<sup>15</sup> are generally useful only as far from the source and are not exploited further. More complicated velocity profiles have not been treated, but qualitative and semiquantitative extensions of the above results are possible if the velocity fields can be defined.

Velocity fields around a sphere<sup>19</sup> and a cylinder<sup>20</sup> have been calculated and will be discussed later when nozzle drag is considered. Further consideration of other nozzle effects (e.g., Heller's criterion) will be delayed until the discussion of results.

#### Experimental

The test diffusion chamber was a 4-foot length of 21-1/4 cm i.d. stainless steel pipe which was pumped by a Leybold-Heraeus WA 250 Roots-type pump. Pumping speeds of 60 l sec<sup>-1</sup> at 1 torr were attainable, corresponding to average carrier gas velocities of ~ 2 meter sec<sup>-1</sup>.

The nitrogen atmospheric gas flow was measured with a pre-calibrated Matheson tri-flat flow meter. In order to establish laminar flow in as short a distance as possible down the diffusion tube, the atmospheric gas inlet line fed through a brass diffusion plate (3/16" thick) which carried a pattern of fifty 1/32" i.d. holes which delivered mass flows corresponding to the relative fluxes in fully developed parabolic laminar flow. A series of four 14-mesh brass screens were placed with crossed meshing on the surface of the outlet plate to break up wakes at the holes; flow asymmetry, which was correlated with turbulent flow out of the diffuser orifices, was completely eliminated in this manner at distances of the diffuser from the Hg inlet nozzle down to less than 10 cm. However, experiments were routinely done with a diffuser-inlet nozzle distance of roughly 50 cm to encourage development of an atmospheric parabolic velocity profile typical of laminar flow.

The Hg vapor inlet system consisted of a carburetor section and a pulsed inlet section. Nitrogen gas at several torr was passed over hot Hg (~ 70°C) and through a (variable) constant temperature trap containing pyrex wool and droplets of Hg so as to reduce the Hg mercury vapor pressure to the saturation pressure at the desired temperature. The N<sub>2</sub>, Hg mixture flowed into a pulser. The pressure in this section and in the diffusion tube was monitored with a Validyne DP7 pressure transducer. The average flow rate of the N<sub>2</sub> carrier was adjusted and maintained with a fine metering valve and a pressure head constant to better than ± 1/2%, and was measured by the rate of pressure drop from a calibrated volume. The pulsing action arose from the reciprocal motion of a stainless steel rod, whose nylon tip entered a stainless steel nozzle (N) and created a virtual seal; various shaped tips could be attached to N. The pulser body and fittings were of brass, and the internal surfaces were coated with Teflon to protect them against Hg attack. Attached to the driver cam was a sector passing through the path of a photodiode-photo cell unit which provided synchronous trigger signals. Pulsing rates from 0.5 cps to 6 cps were used and were designed with 150 degrees each of "on" and "off" action separated by 30 degree transition regions. Therefore, a period was available, which was as long as about 1 sec per "on" cycle, in order to ensure development of steady-state conditions while transition times as short as 10 msec could be provided. Of course, the ratio of the "on" time to the transition time was constant for the cam.

The relative Hg concentration in the diffusion tube was measured in situ by the absorption of the 2537 Å emission line of a low pressure d.c. powered Ortel model C-13-62 Hg lamp. The lamp was stabilized with a ballast resistor (normally 25-62KΩ) and was housed in a sealed brass cylinder to minimize the effect of air currents on the lamp temperature and output intensity. The radiation from the lamp was monitored by a reference photomultiplier cell.

A short length (< 5 cm) of 3 mm Suprasil rod with polished ends, directed light from the lamp to the reference photomultiplier through an Optics Technology, Inc. interference filter to isolate the 2537 Å line. The lamp radiation was transmitted into the diffusion tube through 500 mm long flexible UV light guide (Schott Optical Glass Inc) with a 1 mm diam bundle. The light guide was mounted to a detector assembly moveable in three dimensions inside the diffusion tube which also carried a receiver guide which intercepted the radiation from the first light guide at a distance of 1 cm; this rather large path length was selected in order to minimize local flow perturbations in the sampling region. This receiving guide fed to a second photomultiplier housing with an interference filter (Optics Technology Inc.) with 6% transmission at 2537 Å.

The signals from the monitoring and the reference photomultiplier were each pre-amplified, filtered ( $\tau = 1$  msec) and fed into a differential amplifier. The difference signal could be amplified by up to 4 additional factors of 10 and could either be routed to a recorder or to the input of a Varian model C-1024 CAT. The scan of the CAT was synchronized to the pulsing action of the cam by the trigger method described above. The rate of address advance was controlled by an external timebase with a 100 kHz internal standard clock. The stored signal in the CAT could be recorded on the chart recorder. In this way both the magnitude and the time development of the pulses were measured.

The Hg detector could be moved relative to the Hg source in three dimensions. The vertical displacement could be estimated to 0.2 mm. The angular displacement of the detector in the horizontal plane was determined to less than 0.2°. With a maximum lever arm, this corresponded to an uncertainty of < 1 mm in the distance between the detector center and the Hg inlet.

The accuracy of the detector alignment was calibrated by observations with a cathetometer. It was determined that the axial detector motion deviated

from true axial motion in a vertical plane by  $\pm 2.0^\circ$  and in a horizontal plane by  $0.3^\circ$ . The maximum deviations of the direction of detector support motion to the radial direction were estimated to be less than  $0.1^\circ$  in the vertical axial plane and  $0.2^\circ$  in the radial plane. Corrections were routinely made for the axial deviations where appropriate; the other deviations are considered to be negligible.

The percent absorption,  $A$ , of the Hg 2537 Å radiation was used to determine relative Hg concentrations over a range corresponding to absorptions of about 0.3% to greater than 5%. The results were fitted by least squares to Beer's law. The law gave fit with absorption coefficient  $\epsilon = 1.65 \times 10^{14} \text{ cm}^2 \text{ atom}^{-1}$  and a coefficient of correlation greater than 0.99. At low absorptions, Beer's law predicts that  $A$  is proportional to the concentration. At higher  $A$ , Beer's law was used to determine the relative Hg concentration.

## RESULTS AND DISCUSSION

A. Inlet nozzle configuration

Steady state concentration profiles were determined with the use of various Hg vapor inlet nozzles. Comparison of the results provides information regarding the effect on substrate spatial distribution of source type and configuration, inlet flow velocity, atmospheric gas flow velocity, pressure, shadowing and drag effects, etc.

Radial tubular nozzles

Two different sized nozzles, N-1(1 mm id) and N-2(2 mm id), were used in a vertical radial configuration with the nozzle tip terminating at the axis of the diffusion tube. Thus, the issuing  $N_2$ , Hg mixture enters the  $N_2$  atmospheric flow in the positive  $\rho_v$  direction with these nozzles.

One set of measurements was made of concentration profiles along the  $z$  axis downstream of the nozzle ( $R = z$ ). Equation IV predicts that for the nonre-active case, the concentration should be proportional to  $z^{-1}$  along the axis. Figure 1 shows that the experimental relative substrate concentration data follow the predicted behavior for  $z^{-1} < 1.0 \text{ cm}^{-1}$ . An apparent curvature at greater values of  $z^{-1}$  is largely experimental artifact. It is in part a consequence of the finite detector sample path (1 cm). The atmospheric flow effect which appears as  $\exp[U(z-R)/2D]$  (eq. IV) is unity on axis ( $R = z$ ), but is considerably less than unity at constant  $\rho$ , for  $z^{-1} > 1 \text{ cm}^{-1}$ . Thus, averaging over the detector path length in  $\rho_v$  results in an average "observed" concentration less than the true axial concentration. The ostensible values of  $U/2D$ , measured as described below, lead to average observed concentrations at  $z^{-1} > 1$  which are at least 8% below the deduced true axial concentrations. The latter are shown as solid circles in Fig. 1.

Another source of error in the measurements at high  $z^{-1}$  is the determination of the precise detector location. An absolute error of 0.05 cm in  $z$  (comparable to the radii of the nozzle and the fiber optics) at 1 cm can result in a 5% error in  $z^{-1}$  (error bars in Fig. 1).

It is concluded that the axial concentration profiles are well behaved within the experimental uncertainty.

The concentration profiles in the transverse direction (constant  $z$ ) should depart from an  $R^{-1}$  dependence away from the axis ( $R > z$ ) due to the exponential factor in eq. IV. Figures 2 and 3 show experimental results at  $z = 2$  and 4 cm, respectively, for measurements in the  $\pm \rho_v$  direction. The solid lines represent calculated profiles of the form  $[AR^{-1} \exp[B(z-R)]]$ , where  $A = 1/4D$  and  $B = U/2D$ . The figures reveal an asymmetry; the concentration falls off less steeply in the negative  $\rho_v$  direction. This is a consistent observation, with  $B^- = 0.5 B^+$ , where  $B^\pm$  are the values of  $B$  required to fit the negative and positive wings, respectively. The values of  $B$  are proportional to the total atmospheric mass flow rate  $Q$  (since  $U/D \propto Q$ );  $B^+ = 1.8 (\pm .15) \times 10^{-2} Q \text{ cm}^{-1}$  at  $22^\circ \text{C}$  was measured for both nozzles. The individual values of  $U$  and  $D$  are described below.

By contrast, transverse concentration profiles in a horizontal plane (Fig. 4) are comparatively symmetrical about the axis. We infer that the nozzle tube, itself, which lies along the negative  $\rho_v$  axis, caused a perturbation of the flow-diffusion process. This phenomenon may be understood in terms of the distortion of the atmospheric flow stream by the nozzle which has a 6.4 mm o.d. terminating in a 1.3 cm length with an o.d. of 3.2 mm. Under typical experimental conditions ( $U \sim 100 \text{ cm sec}^{-1}$  at about 1 torr), these dimensions correspond to Reynolds numbers,  $Re$ , less than 1. Allen and Southwell<sup>20</sup> have determined the 2-dimensional flow of a fluid past a circular disc by use of relaxation methods to solve the Navier-Stokes equation for viscous flow. The resulting stream

functions for  $Re = 1$  were applied here to extract velocity information which indicated that in a transverse plane, two or three nozzle-diameters downstream of the inlet, the coaxial velocities vary from  $U_f/2$ , on axis, to  $U_f$ , at 3 or 4 diameters off axis; here,  $U_f$  is the free stream velocity. Thus, the effective axial velocity downstream of the nozzle is less than the free stream velocity. (The diffusion coefficient will not be affected as standing eddies should not appear at  $Re$  less than 2.)<sup>21</sup> Since  $B$  is proportional to  $U$ , a lower  $U$  should lead to less rapid transverse fall-off of the concentration, as observed. This perturbation of the flow stream extends somewhat into regions of  $\rho_v > 0$ , but is assumed here to be relatively smaller.

#### Nozzle velocity. The effect on the concentration profiles of the inlet

flow parameters was investigated in terms of the ratio of the average nozzle exit velocity  $v_n$  and the Hg diffusion coefficient  $D$  estimated from Lennard-Jones parameters for Hg and  $N_2$ .<sup>22</sup> (See below.) At low values of  $v_n/D$  no dependence of the transverse profiles on this ratio was observable. However, at higher values, the location of the concentration maximum shifted off axis towards positive  $\rho_v$ , as illustrated in Fig. 1. A concomitant change in shape is observed. The shifts of the concentration maxima are plotted as functions of  $v_n/D$  for the two nozzles in Fig. 5. The shift occurs at higher values of  $v_n/D$  for the smaller nozzle than for the larger nozzle, in agreement with the predictions of Reed and Rabinovich<sup>6</sup> and of Mintz and LeRoy.<sup>7</sup> The values of  $v_n/D$  were  $17\text{ cm}^{-1}$  for N-2 and  $36\text{ cm}^{-1}$  for N-1; these are in good agreement with the respective values of 14 and  $28\text{ cm}^{-1}$  calculated from the equation of Mintz and LeRoy ( $v_n/D = \sqrt{2}/r_0$ , where  $r_0$  is the nozzle radius).

An additional observation was that the displacement  $\delta$  increased more rapidly with  $v_n/D$  for the larger nozzle N-2. In fact, the ratio of the slopes is the ratio of the nozzle radii, roughly two. This behavior may be correlated with momentum effects. The nozzle gas at density  $\rho_n$  enters the system with excess

p. 17 a

momentum  $p_n$  in the positive  $\rho_v$  direction and input momentum rate,  $\dot{p}_n' = \pi r_0^2 v_n^2$ . The mass of atmospheric gas which must absorb this momentum within a distance  $\delta$  is proportional to the density  $\rho_a$ , the atmospheric velocity  $U$ , and the cross-sectional area  $\pi \delta^2$ . Considering only molecular momenta of the atmospheric gas, the intrinsic momentum input rate in the nozzle region is  $\dot{p}_a' \sim \pi \delta^2 \rho_a U \bar{c}$ , where  $\bar{c}$  is the mean molecular speed. The requirement  $\dot{p}_a' \gg \dot{p}_n'$  gives  $v_n/\delta \ll r_0^{-1} (\bar{c} U \rho_a / \rho_n)^{1/2}$ . The densities  $\rho_a$  and  $\rho_n$  refer to the same pressure, so that  $v_n/\delta \ll r_0^{-1} (\bar{c} U M_a / M_n)^{1/2}$ , where  $M$  is the molecular weight of the gas. The slopes given in Fig. 5 correspond to  $\delta D/v \gg [r_0 D / (\bar{c} U M_a / M_n)^{1/2}]$ . This term is typically  $3 \times 10^{-3}\text{ cm}^2$  for N-2, which is about 1% of the experimental value of  $0.32\text{ cm}^2$ , in agreement with the inequality. The momentum argument leads to the prediction that the slopes  $\delta D/v_n$  are proportional to  $r_0$  as observed. The slopes are also predicted to be proportional to  $(M_n / M_a)^{1/2}$ . An experiment was done with He as the nozzle carrier gas and  $N_2$  as the atmospheric gas using the larger nozzle N-2. The solid triangle in Fig. 5, at high  $v_n/D$ , represents the observed vertical shift (compared to that for the top curve.) The shift was even less than that for the smaller nozzle N-1 (lower curve), indicating a momentum effect less than one-half that for  $N_2$  under the same conditions. This is in excellent agreement with the predicted mass effect,  $(4/28)^{1/2} \sim 0.4$ . We propose that the  $v_n/D$  criterion of Mintz and LeRoy be modified with a mass factor;  $v_n/D = \sqrt{2} v_a^{1/2} / r_0 M_n^{1/2}$ . Momentum arguments point up an advantage of a multi-inlet spherical source whereby the nozzle momentum is more symmetrically distributed in direction. Other features of spherical sources are considered below.

p. 18

### Axial tubular nozzle

The radial inlet described above was modified by an axial tubular extension ~ 6 cm in length. The radial flow disturbance described above was thus transferred upstream of the inlet.

Axial concentration profiles were well behaved, as with the radial nozzles. Moreover, transverse profiles along the  $\rho_v$  axis now showed (Fig. 6) substantially improved symmetry about the axis with  $B^{\pm} = 1.4 (\pm .2) \times 10^{-2} Q$ , intermediate between the extremes found with the radial nozzles. This indicates that in a 6 cm distance, the radial nozzle perturbation had spread "evenly" above and below axis and was manifested as an average effect. However, another process may be important here. This involves the drag effect of the nozzle on the atmospheric flow.

Drag effects. The velocity profile for flow in an annular cylinder of length  $l$  and of outer and inner radii,  $r_1$  and  $r_2$ , respectively, is given by<sup>23</sup>

$$U(r) = \frac{\Delta P}{4\eta l} \left[ r_1^2 - r^2 + \frac{(r_1^2 - r_2^2) \ln(r/r_1)}{\ln(r_1/r_2)} \right] \quad \text{XIX}$$

where  $\Delta P$  is the pressure drop along  $l$  and  $\eta$  is the gas viscosity.  $\Delta P$  can be determined from the mass flow  $Q$ ,<sup>23</sup>

$$Q = \frac{\pi \Delta P}{8\eta l} \left[ r_1^4 - r_2^4 - \frac{(r_1^2 - r_2^2)^2}{2 \ln(r_1/r_2)} \right] \quad \text{XX}$$

Here,  $r_2$  is the external radius of the axial nozzle (0.15 cm) and  $r_1$  is the internal reactor radius (10.6 cm). Integration of the velocity profile from  $r=0.015$  to  $r=0.3 r_1$ , weighted by the area element  $2\pi r dr$ , shows that the average mass transport in this region for the coaxial case is about 0.75 that for the full parabolic profile. The region  $0 \leq r \leq 0.3 r_1$  roughly corresponds to the region of measurement illustrated in Fig. 6, where  $B$  (axial)  $\approx 0.8 B^{\pm}$  (radial), the proportionality being similar to the calculated transport factor 0.75.

If the lower  $B$  value for the axial nozzle is indeed due to the nozzle drag, the effect should exhibit cylindrical symmetry. This was tested by several horizontal scans along  $\rho_h$  at  $\rho_v = 0$ ,  $+1.8$ , and  $-1.7$  cm, all at the approximate axial value of  $z = 2$  cm. A consequence of the experimental arrangement of the detector support was that the orientation of the detector relative to the line of centers between the source and detection region was not constant, but varied by  $\pm 10^\circ$ . Due to this correction, all the measurements were not as accurate as those made at  $\rho_h = 0$ . But, in any case, no asymmetry was observed. Values of  $B$  for all three settings of  $\rho_v$  were essentially equal with an average value  $B = 1.3 (\pm 0.2) \times 10^{-2} Q$ , in good agreement with the values for the vertical profiles presented earlier. This supports the proposed source of the distortion of the velocity field, but does not preclude the possibility of a symmetrical spreading of the radial nozzle perturbation at large distances, as previously mentioned. Direct measurements of the velocity gradients in the region of the nozzle structures would be extremely difficult to make at these low pressures.

### Spherical source

The characteristics of a spherical source were investigated. One source (S-1) was a nickel sphere, diameter 1.4 cm, with twenty-four 0.034-cm holes placed in a symmetrical pattern and supported on a vertical feed tube, 0.64 cm o.d. Axial concentration profiles were measured and plotted (not shown) as a function of  $z^{-1}$ . Straight line behavior at  $z > 1$  was again observed; a small positive intercept may indicate a minor artefactual effect of reflection from the walls of the diffusion tube at large  $z$ .

Transverse concentration profiles in the  $\rho_y$  direction exhibited the same type of asymmetry as was observed for the vertical tubular nozzle, with  $B^+ = 0.5 B^-$ , again, and with B magnitudes two-thirds of the tubular values.

A smaller spheroidal nozzle (S-2),  $\sim 0.85$  cm in diameter, was also tested. It had twenty holes (0.018 cm diam.) directed towards the midpoints of the faces of an icosahedron. Transverse profiles with this nozzle were similar to those with S-1, but the B values were closer to those for the tubular nozzle;  $B^+ = (1.4 \pm 0.1) \times 10^{-2} Q$ ,  $B^- = (0.8 \pm 0.1) \times 10^{-2} Q$ . The vertical nozzle support was used with the spherical nozzles and is presumably the major cause of the asymmetry along the  $\rho_y$  axis.

The significantly lower B values obtained with spherical sources is due to perturbation of the velocity field by the spheres. However, even an ideal non-perturbing spherical source is not expected to precisely simulate a point source and we consider this before examining distortions of the velocity field.

The concentration contour at some average small distance ( $\sim 1/2$  cm) from a point source in a flowing atmospheric gas is elongated in the z direction and centered somewhat downstream; for  $U = 100$  cm sec $^{-1}$  the downstream shift is  $\sim 0.1$  cm. Velocity perturbations aside, relative to a point source contour the spherical surface source of radius  $r_s$  tends to introduce more substrate in the region ( $z = 0, \rho = r_s$ ) and less substrate along the downstream axis ( $z = r_s, \rho = 0$ ), i.e. exhibit a more spherical contour. This effect results in lower apparent B values when the data are treated on a point source basis.

A quantitative measure of these effects was obtained by approximate (App. I) computer simulations of a spherical surface source. Semi-quantitative predictions were that axial concentrations converge to those for a point source within 2-3 cm downstream, and that transverse profiles two centimeters

downstream may result in a 5-10% decrease in the apparent B values.

We now return to a consideration of the distortion of the atmospheric velocity field. Under typical experimental conditions, the flow past S-1 corresponded to  $Re \sim 4$ . For a sphere, standing eddies are not observed for  $Re \leq 20$ .<sup>21</sup> By a relaxation technique, Jensen<sup>19</sup> has calculated the stream function around a sphere in a cylinder with a diameter six times that of the sphere. For  $Re = 5$ , the ratio of the axial velocity ( $U_z$ ) in the plane  $z = 0$  to the free stream velocity ( $U_\infty$ ) increases from zero at  $\rho = r_s$  to about 0.5 at  $\rho \sim (1.3-1.4)r_s$ , and roughly 0.9 at  $\rho = 2r_s$ . Results for  $Re = 10$  and 20 indicate that in this range, these relations remain roughly constant.

On this basis,  $U_z \sim 0.5 U_\infty$  at  $\rho = 1$  cm for S-1, and at  $\rho = 0.6$  cm for S-2. The flow lines follow the surface of the sphere with some elongation downstream. Diffusional transport is more important in regions of low velocity; hence, a spherical surface source under these flow conditions may couple with the velocity field to behave like a somewhat larger source. The consequences of this is an increase in the departure from ideal point source behavior mentioned in connection with the computer simulations of a spherical source. The departure results in even lower apparent B values, in agreement with the observed behavior.

In an effort to examine experimentally the effect of the physical presence of the source and the resultant distortion of the atmospheric flow, a 1.4 cm diameter sphere with one axial orifice was used in two configurations, the outlet alternatively faced the  $-z$  and  $+z$  directions. Transverse measurements were made at  $z = 5$  cm corresponding to axial displacements from the source of 5.7 cm and 4.3 cm for the respective configurations. In both cases, the above axis concentration wings had B values significantly greater than the value found with S-1. For the upstream

configuration,  $B = 1.4 \times 10^{-2}$  Q, and for the downstream configuration,  $B = 2 \times 10^{-2}$  Q. The difference in these two values is attributed to the requirement that substrate from the upstream nozzle must flow around the sphere and hence is spread out in the  $v_y$  direction, while the downstream axial substrate concentration is reduced. For the downstream nozzle, the sphere acts only as a barrier to back-diffusion and the B value is accordingly higher. The reasonable magnitudes of the B values indicate that no unconsidered gross flow perturbations are present and, therefore, the conceptual employment above of a nonperturbing spherical source is of useful descriptive value.

#### Some Conclusions

The transverse Hg concentration profiles provide information on the local effects of various source configurations. The trends are clear; in general, the higher the B value, the more closely an ideal point source in an unperturbed flow field is approximated. In order to better appreciate the significance of experimental values of B, we have expressed them in terms of specific values of U and D.

Literature values of the binary diffusion coefficient of Hg vapor in nitrogen, adjusted to atmospheric pressure, are  $0.13 \text{ cm}^2 \text{ sec}^{-1}$  at  $20^\circ\text{C}$  and  $0.16 \text{ cm}^2 \text{ sec}^{-1}$  at  $25^\circ\text{C}$ . From tabulated<sup>22</sup> Lennard-Jones parameters and the collision integrals  $\Omega_{1,2}^{(1,1)*}$ , the diffusion coefficient may be calculated from the Chapman-Enskog theory to be  $0.13$  to  $0.14 \text{ cm}^2/\text{sec}$  at  $25^\circ\text{C}$  (and roughly proportional to the square of T). The mean value was adopted:  $D \approx 0.14 \text{ cm}^2 \text{ sec}^{-1}$  at  $25^\circ\text{C}$ . The value of U corresponding to the axial velocity of a laminar stream in a cylinder is simply twice the experimentally determined average flow velocity. In terms of these values of U and D, we define a relationship for  $B_p$ , the theoretical value of B on axis in the case

of parabolic flow, which is found to be  $B_p = 2.06 \times 10^{-2}$  Q at  $22^\circ\text{C}$ . We define the reduced value,  $B_r = B/B_p$ , which measures the adherence to the idealized parabolic behavior. Values of  $B_r$  for various nozzles are given in Table I for comparison.

A number of conclusions can be drawn from Table I. The presence of a radial nozzle or nozzle support introduces a significant perturbation downstream which leads to asymmetric profiles; an axial nozzle does not. However, the largest value of  $B_r$  (close to unity) was measured above the axis for the radial tubular nozzle. This result indicates the minimum atmospheric flow perturbation, and hence the radial nozzle appears to be more useful than the axial one, especially for measurements in the  $v_y$  direction and very close to the nozzle where uncertainties in the flow perturbation could strongly affect data interpretation.

In the study of unimolecular reactions, a radial inlet may be preferable for another reason. The reactant gas must be kept cool until it enters the hot atmospheric stream, and the inlet nozzle portion, at least, will be significantly cooler than the atmospheric gas. The radial arrangement tends to minimize any temperature perturbations in the region of chemical interest.

Spherical nozzles have the advantage of multi-jet input, but this advantage is countered by the resulting "artificial" (arising from its finite size) decrease in  $B_r$ . In addition, a considerable perturbation of the atmospheric flow by the sphere is introduced. The greatest utility of the spheres is for measurements substantially removed from the spheres ( $z > 2\text{-}3 \text{ cm}$  under typical conditions) and at low velocities where the diffusional process predominates. This utility would increase as the source size is decreased, as evidenced by the higher  $B_r$  values for S-2.

### B. Time Profiles

In order to obtain rate information from concentration profiles in a reacting system, each position must be correlated with a reaction time. For a flat velocity profile, the reaction process may be directly included in the overall solution (eq. IV) of the continuity equation. In a real, non-idealized system, this is not generally feasible a priori. Therefore, we have made direct measurements of the time development of concentration at various locations relative to the source. We show that use of the measured value of  $U$  yields the observed time profiles and may, in principle, be used with eq. IV to obtain rate constants for reactive data.

#### Experimental Time Profiles

The time-dependent behavior for diffusion from a point source with no reaction has been presented in eq. IX ( $k=0$ ). Comparison with the steady-state expression (eq. IV) leads to the result,

$$C(z, R, s) = C(z, R) \left[ \frac{1}{2} \exp\left(\frac{UR}{D}\right) \operatorname{erfc}\left(\frac{R+Us}{2\sqrt{Ds}}\right) + \frac{1}{2} \operatorname{erfc}\left(\frac{R-Us}{2\sqrt{Ds}}\right) \right] \quad (XXI)$$

The bracketed terms describe the evolution to steady-state. When  $R=Us$ , the right hand term equals 0.5 and the left hand term (expressed as  $\frac{1}{2} \exp\left(\frac{UR}{D}\right) \operatorname{erfc}\left(\sqrt{\frac{UR}{D}}\right)$ ) becomes relatively small at large  $UR/D$ . At large  $R$ , a plot of  $s_{1/2}$ , the time to reach 50% of the steady-state concentration, vs  $R$  should be a straight line of slope  $U$ . In fact, for  $R > 2$  cm, this linear relationship holds well (within a few percent) down to  $U/D \sim 1$  and has the advantage of yielding  $U$  directly as shown below. First, however, the full profiles (eq. XXI) were utilized.

Full time profiles: The experimental time profiles were analyzed to determine values of  $U$  and  $D$ . Linear least squares fits of the data to

eq. XXI were computed for two sets of variables. In one case,  $D$  was fixed and best values of  $U$  and  $s_0$  (the time delay from the CAT trigger to the start of the Hg pulse) were computed. In the other case,  $s_0$  was fixed and  $U$  and  $D$  were fitted to the data. In this way it was possible to test various aspects of the treatment of the data. A summary of the findings follows.

$D$  fixed. Equation XXI is based on a step function source. The actual time profile was measured at  $z=0$  and a number of profiles were also measured at different  $z$  under constant experimental conditions. They were fitted to three different input models: a single-step function, and four- and eight-step functions which simulated the experimental profile at  $z=0$ . Some results are illustrated in Table II. Except for profiles at low  $z$ , the shape of the input function has negligible effect on the best-fit values of  $U$ . The differences in  $s_0$  for the different models are roughly the same for all profiles and correlate with the shift in the "half-on" time for the particular model. Since the increased computational time for the multistep input functions was small, they were routinely used in subsequent fits.

$s_0$  fixed. The sensitivities of  $U$  and  $D$  to fixed input values of  $s_0$  differed considerably. For example, for a profile at  $z=5$  cm, when  $s_0$  was changed by  $\pm 10$  msec, the computed values of  $U$  varied by  $\pm 10\%$  while  $D$  varied by  $\pm 40\%$ . Thus,  $U$  can be fairly well established by selecting an  $s_0$  which results in a reasonable value of  $D$ .

The final fitting of the profiles at various  $z$  was made by fixing  $s_0$ . Least-squares values for  $U$  and  $D$  were computed; some experimental fits are given in Table III;  $s_0$  was set at 25 msec, the average of the values for the eight-step ramp in Table I. The profiles far from the nozzle ( $R > 3$  cm) yield consistent values of  $U(125 \pm 7 \text{ cm sec}^{-1})$  and  $D(90 \pm 10 \text{ cm}^2 \text{ sec}^{-1})$ , except for the profile below axis ( $s_0 = -4$  cm) which fits a lower value of  $U$  and a higher value of  $D$ ;

this may be an artifactual consequence of the perturbed velocity field. Correction of  $D$  to atmospheric pressure gives the value  $D = 0.11 \pm 0.01 \text{ cm}^2 \text{ sec}^{-1}$ , in fair agreement with the value  $0.14 \text{ cm}^2 \text{ sec}^{-1}$  adopted earlier. From the ratio  $U/D$  derived from the least squares fitting,  $B_r$  is determined to be  $0.9 \pm 0.1$  for the radial tubular nozzle, in good agreement with the above-axis value  $B_r^+ = 0.87 \pm 0.07$  in Table I. The time profile measured below axis is fitted with a lower  $B$  value, a trend noted also for the concentration profiles in the table.

Time delays: Experimental values of the time delay from the CAT trigger to the development of 50% steady-state concentration at various axial distances from the radial tubular nozzle were plotted as a function of  $R$  (Fig. 7). Good straight-line behavior is exhibited. The slope yields  $U = 138 \text{ cm sec}^{-1}$  which is about 80% of the axial value predicted for parabolic flow from the measured average value  $\bar{U} = 87.5 \text{ cm sec}^{-1}$ . This agrees well with the value  $125 \pm 7 \text{ cm sec}^{-1}$  determined from the full profiles and is more accurate. (From trends previously described, a higher  $U$  would result in a higher  $S_0$  and a higher  $D$  in the fitting. The calculated value of  $B_r$  would tend to decrease. These effects would all improve the agreement of  $D$  with the adopted value, and of  $B_r$  with the value determined from concentration profiles). The open and closed circles in Fig. 7 represent off-axis results at  $z=3 \text{ cm}$ , and  $\rho_v = \pm 4 \text{ cm}$ , respectively ( $R = 5$ ). The time delay above axis is the same as on axis but is greater below axis. This can be related to a lower effective velocity in the region of negative  $\rho_v$ , a description which agrees with the observation of low  $B^-$  values with radial nozzles.

Time delay measurements were also made at  $z = 0$  where nozzle perturbations would be minimal (Fig. 8). Definite curvatures are observed. At low  $\rho_v$ , this is a result both of the non-linearity of  $R$  with  $U$  (eq. XXI) and of the finite detector path length. The results for  $\rho$  between 2 to 5 cm, yielded a constant

value  $U = 62 \text{ cm sec}^{-1}$  which is  $\sim 70\%$  of the predicted axial parabolic velocity as determined by the average flow rate. The curvature at  $\rho_v > 5 \text{ cm}$  is expected, since the parabolic velocity profile decreases to  $0.64 U_0$  at  $\rho = 6 \text{ cm}$ . The (transverse) steady-state concentrations were used to determine a value of  $B_r$ . All data inclusive of the concentration at  $\rho_v = 6 \text{ cm}$  were consistent with  $B_r = 0.80$ , in agreement with the value  $0.87 \pm 0.07$  (Table I).

The implication of this experiment is that the atmospheric velocity field above axis remains constant downstream of the radial nozzle. The effective velocity is lower than that for parabolic flow — either because the expected parabolic profile is never actually established or else is significantly disturbed by the presence of the nozzle.

In addition, the presence of radial velocity gradients could result in averaging of the velocity over regions of excursion of the diffusing substrate. This would also affect transverse concentration profiles, yielding lower  $B$  values. In order to evaluate the influence of velocity gradients, a Monte Carlo method was used to simulate diffusion in several flow fields. The calculation provides a measure of the effect of the flow field on both time-dependent and steady-state concentrations. We briefly describe the calculational model and then discuss the results. Calculational details can be found in App. 2.

#### Monte Carlo Simulation of Velocity Gradients

The simultaneous diffusional and convective transports of each particle was treated as a succession of two-step processes: diffusion (a randomly directed step of distance  $\lambda'$ ), followed by flow (a step in the  $z$  direction of magnitude  $u'(\rho)$ , where the  $\rho$ -dependence of  $u'$  is determined by the velocity profile). Each two-step process, termed a diffusion event, corresponds to a particular time interval,  $\tau$ , which relates the magnitudes of  $\lambda'$  and  $u'(\rho)$  for particular  $D$  and  $U$  to be simulated.  $\lambda'$  was small relative to the velocity gradient so that one step did not carry a particle into a region of significantly different velocity.

P particles were started at the origin. The locations of the particles after each diffusion event were recorded as tallies in a two-dimensional position matrix in  $p$  and  $z$ . Particles outside the range of the matrix were not counted but their positions were retained for the next diffusion event. After some  $E_D$  of diffusion events, the position matrix contains about  $PE_D$  tallies (except for those out of range of the matrix) and represents the particle distribution  $\tau E_D$  seconds after the start of the source (intensity  $I = P/\tau$ ). Eventually, at large  $E_D$ , the matrix became invariant with  $E_D$  when the steady-state had been reached.

Appropriate values,  $\lambda'$  and  $u'(\rho)$ , were selected to relate the simulation to  $D$  and  $U(\rho)$  in terms of the tube radius  $\rho_0$  (10 cm) and the characteristic time  $\tau (\sim 1 \text{ msec})$ . It is easily seen that  $u'(\rho) = \tau U(\rho)$ . Chandrasekhar<sup>26</sup> has shown that, for pure diffusion, this model of constant  $\lambda'$  behaves, for a large number of events, like real diffusion with a diffusion coefficient  $D = (\lambda')^2/6\tau$ . In terms of the reduced variable,  $\bar{\rho} = \rho/\rho_0$ , then  $u(\bar{\rho}) = (\tau/\rho_0)U(\rho)$  and  $\sqrt{6\tau}/\rho_0$ . The value of  $\tau$  was chosen so that steady-state was reached for  $E_D \sim 500$ . The parameters used are summarized in Table IV. Four velocity models were employed.

$u(\bar{\rho}) = 0$ . This represents pure diffusion and was used to test the technique. The simulation was performed for two different values of  $\tau$  (Table IV).  $P$  and  $E_D$  were adjusted so that both cases corresponded to the same diffusion time ( $t = E_D \lambda'^2 \rho_0^2 / 6D = 2\rho_0^2/30$ ) and same source intensity ( $I = 6P/\lambda'^2 \rho_0^2 = 4.5 \times 10^7 D/\rho_0^2$ ). The time dependent solution for pure diffusion is

$$C(R,t) = \frac{I}{4\pi DR} \operatorname{erfc}(R/\sqrt{4Dt}) \quad (\text{XXII})$$

This equation can be used (App. 2) with the given values of  $t$  and  $I$  to calculate the populations predicted for the various matrix grains. Figure 9 shows a comparison of the absolute populations calculated by eq. XXII with the computer

simulated values for matrix elements  $V_{5,2}$  (App. 2). Excellent agreement is evident, especially for  $\lambda = 0.02$ . The apparent larger scatter for  $\lambda = 0.01$  may be the result of poor statistics for the fewer particles since each particle is followed through its entire trajectory.

These particular simulations were made on ten subsets of  $P/10$  particles. It was therefore possible to obtain a measure of the variation of grain populations for the subsets. The relative fluctuations were about twice as high for  $\lambda = 0.01$  as for  $\lambda = 0.02$ , even though the populations were the same. This indicates that the fluctuations are proportional to  $P^{1/2}$  and independent of  $\tau (\propto \lambda^2)$ .

At the origin ( $V_{1,1}$ ), the theoretical population is about 5300, while  $\lambda = 0.02$  gives 4400, and  $\lambda = 0.01$  gives 5000. With the smaller step size, the region at the source is approximated better. Since our interest was in regions somewhat removed from the source, we elected to use  $\lambda = 0.02$  and  $P = 3000$  for subsequent calculations.

$u(\bar{\rho}) = 2.7 \times 10^{-3}$ . This corresponds to a flat velocity profile with  $U/2D = 2$ . This model provided a check of the method of simulating flow conditions. A large value of  $U$  was chosen to ensure rapid attainment of the steady-state and to create a large effect on transverse concentration profiles.

A steady state was reached over most of the matrix for  $E_D = 400$ . Transverse relative concentration profiles were plotted as  $\ln(R/C)_{\text{rel}}$  vs  $R$ , for which straight line behavior with slope  $-U/2D$  is predicted. Figure 10 shows one such profile for  $z = 3.9 \text{ cm}$ , with a least squares slope of  $-2.07$  (open circles). The agreement with the theoretical slope of  $-2.03$  is excellent. At high values of  $p > 5 \text{ cm}$  ( $R \sim 6.3 \text{ cm}$ ), the deviations are the result of bad statistics since the grain populations drop below one hundred. The time profiles for the approach to steady-state were also compared to theory and are illustrated in Fig. 11 for two locations of equivalent  $R$  ( $z = 1.9 \text{ cm}$ ,  $p = 0.1 \text{ cm}$  and  $z = 0.1 \text{ cm}$ ,  $p = 1.9 \text{ cm}$ ). The profiles are predicted to be the same and both do agree with the theoretical profile. The

calculation thus correctly simulates the combined diffusion and convection processes.

$u(\bar{z}) = 2.7 \times 10^{-3} \frac{(1-\bar{z})}{\bar{z}}$ . This model represents an extreme straight-line ("triangular") velocity gradient, designed to show what effect a velocity gradient would have. A plot of  $\ln(R \cdot C)$  vs  $R$  for  $z = 3.9$  cm is given in Fig. 10. Marked curvature is observed, with a decreasingly negative slope at large  $R$  where  $u(\bar{z})$  is small. The slope in the region  $0 < \bar{z} < 3$  cm is  $-1.72$  which corresponds to  $0.85 U(0)/20$ . Interestingly,  $U$  varies by 30% in this region.

$u(\bar{z}) = 2.7 \times 10^{-3} \frac{(1-\bar{z}^2)}{(1-\bar{z})}$ . This case represents a parabolic velocity field with a maximum axial velocity equal to the velocity used for the flat profile case. The effect of the velocity gradient on axial and transverse concentration profiles and on time profiles was explored. The transverse steady-state behavior is illustrated for  $z = 3.9$  cm in Fig. 10. The values of  $\ln(R \cdot C)_{\text{rel}}$  have been shifted due to the nearly perfect overlap with the data for the flat profile. The least squares slope in the region  $0 \leq \bar{z} \leq 3.3$  cm is  $-1.9\%$ , which is 95% of that found for the flat profile. The velocity varies by 10% in this region and thus the effective  $U/20$  corresponds to the median velocity. In any case, the concentrations on axis are essentially equal for both velocity profiles.

For  $\bar{z} \gg 3$ , there is a significant upward curvature (Fig. 10) due to the increased penetration of the particles into regions of large  $\bar{z}$  (and low  $U$ ). This represents the major qualitative difference observed between the flat and parabolic cases.

With a flat profile these particles would have been swept out; nevertheless, their presence at low concentration in the parabolic case could have negligible effect on the populations near the axis. This is borne out by the simulation. A time profile for  $z = 3.9$  cm is illustrated, along with the flat velocity case. Excellent agreement exists between the two time behaviors and with the theoretical curve based on a flat profile. The discontinuity at 120 msec is apparently a computational artifact. As noted in App. 2, the diffusional behavior in both

cases is identical and therefore the observed agreement shows that the velocity profile differences have negligible effect on the behavior on axis. Far off axis (Fig. 13, for  $z = \bar{z} = 2.9$  cm), the effect of a parabolic profile begins to appear in the time profiles, but is small (maximum deviation  $\sim 5\%$ ) compared to that for the linear profile. This behavior is in good agreement with that of the simulated transverse concentration profile. Evidently, use of a flat profile gives good fit for both concentration and time profiles for  $\bar{z} \sim 3-4$  cm.

Axial concentration profiles for the flat and parabolic profiles from  $z = 0$  to  $z = 5$  cm were essentially identical. Least squares fits of the axial concentrations to  $z^{-1}$ , for  $z > 0.4$  cm, yielded slopes in units of particles of  $3.35 \times 10^4 \text{ cm}^{-2}$  for the flat profile and  $3.33 \times 10^4 \text{ cm}^{-2}$  for the parabolic profile (correlation coefficients  $> 0.99$ ), in good agreement with the theoretical value  $3.58 \times 10^4$ .

These observations all support the proposition that in the types of experiments described previously, a parabolic velocity profile yields data describable within experimental uncertainty in terms of a flat profile with a velocity equal to  $U(0)$ . We conclude that the observation of an effective velocity somewhat less than that calculated for laminar flow is not artifactual, but results from a physically real, low velocity profile in our apparatus. Although we cannot unequivocally identify the source of this behavior, all indications are that it is due to the presence of the nozzle. It follows that if a value of  $U = 0.8 U(0)$  is adopted, the maximum possible error introduced would be 20%.

#### Comparison with Previous Work.

Our results indicate that the criterion of Tal'roze and co-workers<sup>3</sup> (eq XVII) is appropriate for both time-dependent and steady-state measurements. In our simulation at  $z = 3.9$ ,  $U(0)/D = 4$  and  $40z/\pi r_0^2 = 0.5$ , a ratio of 8. Even under these borderline conditions, steady-state and time-dependent concentrations considered off axis were calculated to obey (within  $\sim 5\%$ ) the simple flat profile

equation with a velocity equal to twice the average.

In the Introduction, reference was made to a time-dependent calculation of Jarvis<sup>14</sup> relating to the long arrival time of a sheet of ions in laminar flow. Application of the criterion in eq. XVII to the conditions corresponding to Jarvis' calculation shows that the simple inequality does not even hold. Thus, the low effective axial velocity is likely a consequence of extended diffusion from regions of lower velocity.

Nevrovskii<sup>16</sup> calculated steady-state concentration contours for diffusion of a reactant from a point source into a laminar flow stream and into a flat profile flow stream. His calculations showed a large difference in the axial concentrations for the two cases, with a higher concentration in the parabolic case. For a cylinder of 10 cm radius, his calculation corresponded to  $U(0)/2D = 0.7$  and  $k/D = 0.1$ . At  $z = 6$  cm, he found roughly 40% higher concentration in the parabolic case. Since a parabolic profile involves lower velocities off axis, the time to develop steady-state downstream should be no shorter than that for a flat profile (as illustrated by the calculation of Jarvis). Therefore, one must conclude that the consumption by reaction at 6 cm in the parabolic case would be equal to or greater than that for the flat case. Extrapolation to the case of no reaction (our case) would require an axial concentration in the parabolic case at least 40% higher than that for the flat case. This is in direct contradiction to our Monte Carlo results which show essentially identical axial concentration and time profiles for the two cases. This is not a crucial discrepancy, however, since the relative profiles from Nevrovskii are also essentially the same for both velocity cases out to about 15 cm. For a unimolecular isomerization reaction, the relative depletion by reaction can be determined at any point, and with knowledge of the time history at that point (which we have shown to be experimentally determinable) one is able to derive absolute kinetic information.

Acknowledgement. This work was supported by the Office of Naval Research. We wish to thank Dr. E. Kamaratos for many helpful suggestions and discussions.

# Appendix 1. Simulation of spherical surface source

Two models were simulated with the use of eq. IV in tabulated integration formulae.<sup>18</sup> They were chosen to approximate sources which were transparent or opaque to atmospheric gas flow.

Transparent: Integration formulas for a 6-point (i.e., 6-orifice) and 18-point spheres gave identical axial results for  $z > 2$  cm. The concentrations were below those for a single equivalent point source except for the 6-point sphere at  $z \leq 1.2$  cm (this latter finding being an artifactual result of the small number (6) of subsources). The 18-point sphere was used in most calculations.

Opaque: The integration formula for an 8-point ring of radius equal to or greater than that of the sphere was combined with equally-weighted downstream hemispherical integration formula (adapted from the formula for an 18-point sphere). The ring formula provided an approximation to the sweeping of material around the sphere by the flow stream.

Exact models included a sphere 0.7 cm in radius ("transparent" case) and several ("opaque") combinations: ring (1 cm radius), hemisphere (0.7 and 1 cm radii); and ring and hemisphere both 0.7 cm in radius. The results were not strongly dependent on the model and the relevant trends are summarized in the text.

All the simulations with velocity fields were such that 10 groups of 300 molecules each underwent 10 diffusion events in turn. The random number generation was initiated for each velocity profile with the same seed. Therefore, the diffusion histories of the 3000 molecules were identical for each case; the difference in behavior could therefore be attributable to differences in velocity profiles.

## Appendix 2. Monte Carlo Calculations

This calculation is a simulation of a free molecule in space. The choice of random directions was accomplished by use of GGSPR, a subroutine from IMSL Library 3.<sup>a</sup> This routine generated two independent uniform deviates  $U_1$  and  $U_2$  on the interval  $(-1,1)$ . The coordinates  $X = 2U_1\sqrt{1-S}$ ,  $Y = 2U_2\sqrt{1-S}$ ,  $Z = 1-2S$ , are then formed, where  $S = U_1^2 + U_2^2$ .

In terms of reduced coordinates  $\bar{x}, \bar{y}, \bar{z}$  (e.g.,  $\bar{x} = x/\rho_0$  etc.), the  $i$ th location of a particular molecule is simply  $\bar{x}(\bar{y}, \bar{z})_i = \bar{x}(\bar{y}, \bar{z})_{i-1} + \lambda X(Y, Z)$ . Then  $\bar{z}$  was incremented by  $\Delta \bar{z} = u(\bar{\rho}_i)$ , where  $u(\bar{\rho}_i)$  represents the mass transfer by the atmospheric flow (see text) and is a function of  $\bar{\rho}_i$ , where  $\bar{\rho}_i \equiv \sqrt{\bar{x}_i^2 + \bar{y}_i^2}$ . The coordinates  $\bar{x}_i, \bar{y}_i$  and  $\bar{z}_i$  were stored for the next diffusion event while the  $i$ th location of the molecules was recorded in a grid with volume elements  $V_{k\ell}$  defined by  $0.02(k-1) \leq \bar{z}_k < 0.02 k$ ;  $0.02(\ell-1) \leq \rho_\ell \leq 0.02 \ell$ , where  $1 \leq k \leq 25$ ,  $1 \leq \ell \leq 50$ . For  $\rho_0 = 10$  cm (corresponding to the present apparatus),  $\rho \leq z \leq 5$  cm and  $0 \leq \rho \leq 10$  cm, with grainings of 0.2 cm in either coordinate. The average concentration in a volume element  $V_{k\ell}$  is the ratio of the population  $P_{k\ell}$  divided by the volume,  $\bar{V}_k = \pi(\bar{z}_k - \bar{z}_{k-1})(\bar{\rho}_k^2 - \bar{\rho}_{k-1}^2) = \pi(0.02)^3(2\ell-1)$ . Likewise, theoretical populations could be calculated from the average concentrations calculated from eq. IV. Numerical integration over the entire volume generally yielded average concentrations equal to the concentration predicted at the center of the element. In the region of large gradients ( $(k + \ell) < 4$ ), the two averages could be correlated with small correction factors ( $1 \pm 0.1$ ). Time-dependent populations were calculated using the midpoint of the volume element and multiplied by the appropriate steady state correction factor where necessary.

a. IMSL Library 3 is a product of International Mathematical and Statistical Libraries, Inc.

TABLE I. Comparison of experimental B and reduced  $B_r$  values.

Nozzle <sup>†</sup>	$B \times 100/Q$	$B_r$
N-2 (+) <sup>‡</sup>	$1.8 \pm 0.1^5$	$0.87 \pm 0.07$
N-1 (-)	$0.9 \pm$	$0.44 \pm 0.04$
Axial ( $\pm$ )	$1.4 \pm 0.2$	$0.69 \pm 0.10$
S-1 (+)	$1.2 \pm 0.1$	$0.59 \pm 0.06$
S-1 (-)	$0.6 \pm 0.2$	$0.28 \pm 0.11$
S-2 (+)	$1.4 \pm 0.1$	$0.70 \pm 0.06$
S-2 (-)	$0.8 \pm 0.1$	$0.37 \pm 0.05$

<sup>5</sup> based on  $D = 0.14 \text{ cm}^2 \text{ sec}^{-1}$  at 760 mm Hg

<sup>†</sup> see text for nozzle designations

<sup>‡</sup> (+) and (-) indicate results for  $\rho_v > 0$  and  $\rho_v < 0$ , respectively

TABLE II. Least squares values\* for various n-step input functions.

z (cm)	n=1			n=4			n=8		
	U (cm sec <sup>-1</sup> )	S <sub>0</sub> (msec)	U (cm sec <sup>-1</sup> )	S <sub>0</sub> (msec)	U (cm sec <sup>-1</sup> )	S <sub>0</sub> (msec)	U (cm sec <sup>-1</sup> )	S <sub>0</sub> (msec)	U (cm sec <sup>-1</sup> )
1	153.6	34.5	249.1	29.1	365.4	29.0	365.4	29.0	365.4
2	86.9	32.8	93.5	27.1	93.4	25.8	93.4	25.8	93.4
2	105.2	32.8	113.1	26.8	113.2	25.6	113.2	25.6	113.2
3	107.1	28.8	111.8	22.9	111.8	21.7	111.8	21.7	111.8
3	107.1	32.6	110.7	26.5	110.7	25.3	110.7	25.3	110.7
6	117.4	31.0	118.7	24.9	118.7	23.7	118.7	23.7	118.7
7	124.5	33.6	125.9	27.6	125.9	26.4	125.9	26.4	125.9
8	128.0	31.5	129.1	25.5	129.1	24.3	129.1	24.3	129.1

\*D fixed at  $90 \text{ cm}^2 \text{ sec}^{-1}$ . The experimental profiles were obtained at 24°C and 0.92 torr total pressure; average flow velocity =  $87.5 \text{ cm sec}^{-1}$ .

TABLE III. U and D from least squares fits\* with  $s_0$  fixed.†

$z(\text{cm})$	$\rho_v(\text{cm})$	$U(\text{cm sec}^{-1})$	$D(\text{cm}^2 \text{sec}^{-1})$
1‡	0	149	25
2‡	0	110	80
2‡	0	92	71
3‡	0	124	143
3	0	109	88
3	4	131	92
3	-4	107	116
4	0	114	87
5	0	121	98
5‡	0	122	100
7‡	0	123	82
8‡	0	131	93
9.6	0	136	98
11	0	127	72

\* Profiles from experiment presented in fig. 6;  $T = 24^\circ\text{C}$ , total pressure = 0.92 torr; average flow velocity =  $87.5 \text{ cm sec}^{-1}$ .

†  $s_0 = 25 \text{ msec}$ , average value for  $n=8$  in Table II.

‡ These profiles are also represented in Table II.

TABLE IV. Relationships of Monte Carlo parameters to physical constants.

Given		Physical Corollaries *				
$\lambda$	$u(0)$	P	$\tau^+$ (msec)	$U(0)^+$ (cm sec <sup>-1</sup> )	$U(0)/2D$ (cm <sup>-1</sup> )	$1/4-D$ (cm <sup>-2</sup> )
0.01	0	750	0.0333	0	0	$3.58 \times 10^4$
0.02	0	3000	0.133	0	0	$3.58 \times 10^4$
0.02	$2.7 \times 10^{-3}$	3000	0.133	202.5	2.025	$3.58 \times 10^4$

\* based on assumed value,  $\rho_0 = 10 \text{ cm}$

† based on assumed value,  $D = 50 \text{ cm}^2 \text{sec}^{-1}$

# References

1. H. V. Hartel and M. Polanyi, *Z. Phys. Chem.* **B11**, 97 (1930).
2. H. V. Hartel, N. Weir and M. Polanyi, *Z. Phys. Chem.* **B19**, 139 (1932).
3. A. F. Dodonov, G. K. Lavrovskaya, V. P. Strunin, and V. L. Tal'roze, *Kinet. Katal.* **7**, 385 (1966).
4. W. Heller, *Trans. Faraday Soc.* **33**, 1556 (1937).
5. D. Garvin, V. P. Guinn, and G. B. Kistiakowsky, *Disc. Faraday Soc.* **17**, 32 (1954).
6. J. F. Reed and B. S. Rabinovitch, *J. Phys. Chem.* **59**, 261 (1955).
7. K. J. Mintz and D. J. LeRoy, *Can. J. Chem.* **53**, 1729 (1975).
8. V. P. Strunin, A. F. Dodonov, G. K. Lavrovskaya, and V. L. Tal'roze, *Kinet. Katal.* **7**, 693 (1966). See also: A. F. Dodonov, G. F. Lavrovskaya, and V. L. Tal'roze, *ibid.* **10**, 22 (1969); **10**, 477 (1969), *Op. Cit.* **10**, 573 (1969); **11**, 677 (1970).
9. Y. M. Gershenzon, F. B. Moyn and Y. P. Yurkevich, *Kinet. Katal.* **16**, 1373 (1975).
10. V. A. Nevrovskii and L. B. Soroka, *Kinet. Katal.* **17**, 551 (1976).
11. R. E. Walker and A. A. Westenberg, *J. Chem. Phys.* **29**, 1139 (1958).
12. M. L. Snow and A. A. Westenberg, *Quart. Progr. Rept., Applied Physics Laboratory, The Johns Hopkins University*, T6331-3 October-December 1959.
13. G. C. Frazier, Jr. and W. J. Kooyman, *Chem. Eng. Sci.* **23**, 353 (1968).
11. L. W. Hart, C. Grunfelder, and R. M. Fustrum, *Combust. Flame* **23**, 109 (1974).
12. A. F. Dodonov, G. K. Lavrovskaya, V. P. Strunin, and V. L. Tal'roze, *Kinet. Katal.* **7**, 385 (1966).
14. S. Jarvis, Jr., *J. Res. Nat. Bur. Stand. Sec. B* **72B**, 135 (1968).
15. R. L. Brown, *Int. J. Chem. Kinet.* **2**, 475 (1970).
16. V. A. Nevrovskii, *Kinet. Katal.* **16**, 823 (1975).
17. H. A. Wilson, *Proc. Camb. Phil. Soc.* **12**, 406 (1904).
18. *Handbook of Mathematical Functions*, edited by M. Abramowitz and I. Stegun, U.S. Department of Commerce and National Bureau of Standards, Applied Mathematics Series 55 (1964).
19. V. G. Jensen, *Proc. Roy. Soc. A* **249**, 346 (1959).
20. D. N. G. Allen and R. V. Southwell, *Quart. J. Mech.* **8**, 129 (1955).
21. M. VanDyke, "Perturbation Methods in Fluid Mechanics," Academic Press, New York, N.Y., 1964.
22. J. O. Hirschfelder, C. F. Curtiss, and R. B. Bird, "Molecular Theory of Gases and Liquids," John Wiley and Sons, Inc., New York, N.Y., 1964.
23. J. Happel and H. Brenner, "Low Reynolds Number Hydrodynamics," Prentice-Hall, Englewood Cliffs, N.J., 1965.
24. J. M. Mullaly and H. Jacques, *Phil. Mag.* **48**, 1105 (1924).
25. J. L. Spier, *Physica* **7**, 381 (1940).
26. S. Chandrasekhar, *Rev. Mod. Phys.* **15**, 1 (1943).

# Figure Captions

Fig. 1 Open circles show plot of relative axial (i.e.,  $R = z$ ) Hg concentration as a function of  $R^{-1}$  for radial nozzle N-1,  $T = 28^\circ$ , total pressure = 1.52 torr,  $\bar{U} = 106 \text{ cm sec}^{-1}$ . Filled circles represent values corrected for finite detector path length. Error bars indicate uncertainty in  $z^{-1}$  corresponding to an uncertainty in  $z$  of  $\pm 0.05 \text{ cm}$ .

Fig. 2 Experimental vertical Hg profiles (arbitrary units) at  $z = 2 \text{ cm}$  for radial nozzle N-2,  $T = 22^\circ$ ;  $\bigcirc$ ,  $Q = 37.5 \text{ atm cc sec}^{-1}$ , total pressure = 1.43 torr,  $\bar{U} = 113 \text{ cm sec}^{-1}$ ,  $v_n/D = 4.7 \text{ cm}^{-1}$ ;  $\bullet$ ,  $Q = 37.1 \text{ atm cc sec}^{-1}$ , total pressure = 1.60 torr,  $\bar{U} = 100 \text{ cm sec}^{-1}$ ,  $v_n/D = 38 \text{ cm}^{-1}$ . Solid curve represents fits to the open circles based on  $B^+ = 1.8 \times 10^{-2} Q$  for  $\rho_v > 0$ , and  $B^- = 1 \times 10^{-2} Q$  for  $\rho_v < 0$ . Calculated curves include corrections for finite detector path length.

Fig. 3 Vertical Hg profile (arbitrary units) at  $z = 4 \text{ cm}$  for radial nozzle N-2,  $T = 22^\circ$ ,  $Q = 37.5 \text{ atm cc sec}^{-1}$ , total pressure = 1.43 torr,  $\bar{U} = 113 \text{ cm sec}^{-1}$ ,  $v_n/D = 4.7 \text{ cm}^{-1}$ . Solid curves represent calculated profiles (corrected for finite detector path length) based on  $B^+ = 1.8 \times 10^{-2} Q$  for  $\rho_v > 0$ , and  $B^- = 1 \times 10^{-2} Q$  for  $\rho_v < 0$ .

Fig. 4 Horizontal Hg profile (arbitrary units) at  $z = 4 \text{ cm}$ . Same experiment as in Fig. 3. Solid curves represent calculated profiles (with corrections for finite detector path length) based on  $B = 1.3 \times 10^{-2} Q$ .

Fig. 5 Plot of apparent vertical shift in maximum of vertical concentration profile at  $z = 2 \text{ cm}$  as a function of  $v_n/D$  (see text). Conditions were nearly constant with total pressures around 1.5 torr  $N_2$  and  $\bar{U} \sim 100 \text{ cm sec}^{-1}$ .  $\bigcirc$ , radial nozzle N-1; slope at large  $v_n/D$  equals  $0.17 \text{ cm}^2$ .  $\Delta$ , radial nozzle N-2, slope at large  $v_n/D$  equals  $0.32 \text{ cm}^2$ .  $\blacktriangle$ , radial nozzle N-2 with He as nozzle gas.

Fig. 6 Vertical Hg profile (arbitrary units) at  $z = 2 \text{ cm}$  for the axial nozzle,  $T = 23^\circ$ ,  $Q = 34.8 \text{ atm cc sec}^{-1}$ , total pressure = 1.53 torr,  $\bar{U} = 98 \text{ cm sec}^{-1}$ ,  $v_n/D = 14.6 \text{ cm}^{-1}$ . Solid curves represent calculated profiles (with corrections for finite detector path length) based on  $B = 1.4 \times 10^{-2} Q$ .

Fig. 7 Experimental delay times from CAT trigger to half height of Hg pulses as a function of distance  $R$  from source for radial nozzle N-1,  $T = 24^\circ$ , total pressure = 0.92 torr,  $\bar{U} = 175 \text{ cm sec}^{-1}$ ,  $v_n/D = 40 \text{ cm}^{-1}$ ;  $\Delta$ , axial data ( $z = R$ ,  $\rho_v = 0$ );  $\bigcirc$ , above axis data ( $z = 3 \text{ cm}$ ,  $\rho_v = 4 \text{ cm}$ );  $\bullet$ , below axis data ( $z = 3 \text{ cm}$ ,  $\rho_v = -4 \text{ cm}$ ). Straight line represents least squares fit with inverse slope  $138 \text{ cm sec}^{-1}$  ( $r^2 > 0.99$ ).

Fig. 8 Experimental delay times from CAT trigger to half height of Hg pulses as a function of the radial distance above the nozzle ( $z \approx 0$ ) for radial nozzle N-1,  $T = 27^\circ$ , total pressure = 1.70 torr,  $\bar{U} = 89 \text{ cm sec}^{-1}$ ,  $v_n/D = 46 \text{ cm}^{-1}$ . Straight line represents least squares fit ( $r^2 > .99$ ) of data in the range  $\rho_v = 2\text{--}5 \text{ cm}$ . Inverse slope is  $62 \text{ cm sec}^{-1}$ .

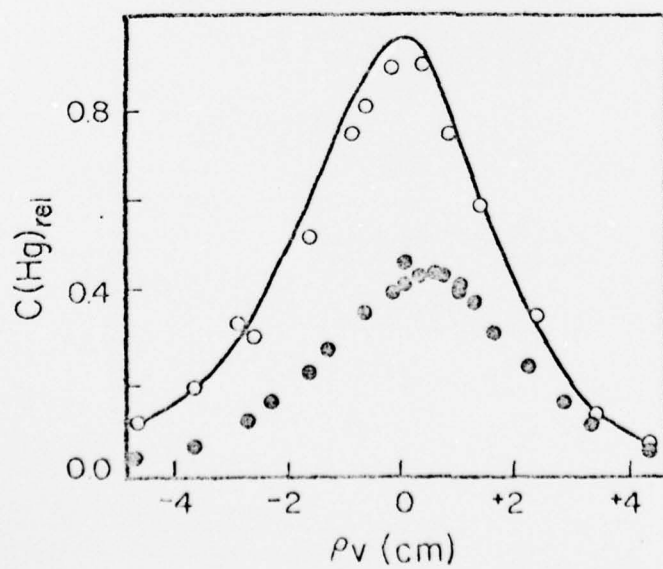
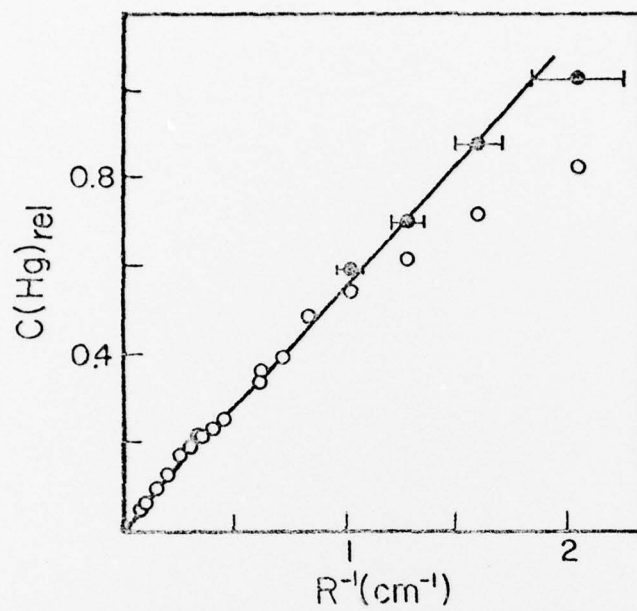
Fig. 9 Monte Carlo calculated populations of grains  $V_{S,L}$  (App. 2) for case of diffusion only ( $u(\bar{\rho}) = 0$ ) from two simulations. In each case the time,  $t$ , corresponds to  $2\rho_0^2/3D$  sec and the source intensity corresponds to  $4.5 \times 10^7 D/\rho_0^2 \text{ sec}^{-1}$ . Specific input values were:  $\bigcirc$ ,  $\lambda = 0.02$ ,  $P = 3000$ ,  $E_0 = 100$ ;  $\Delta$ ,  $\lambda = 0.01$ ,  $P = 750$ ,  $E_0 = 400$ . Solid line is smoothed curve through populations calculated from eq XXII. The peaking of the populations is a result of the increasing volumes  $V_{S,L}$  as  $\lambda$  increases.

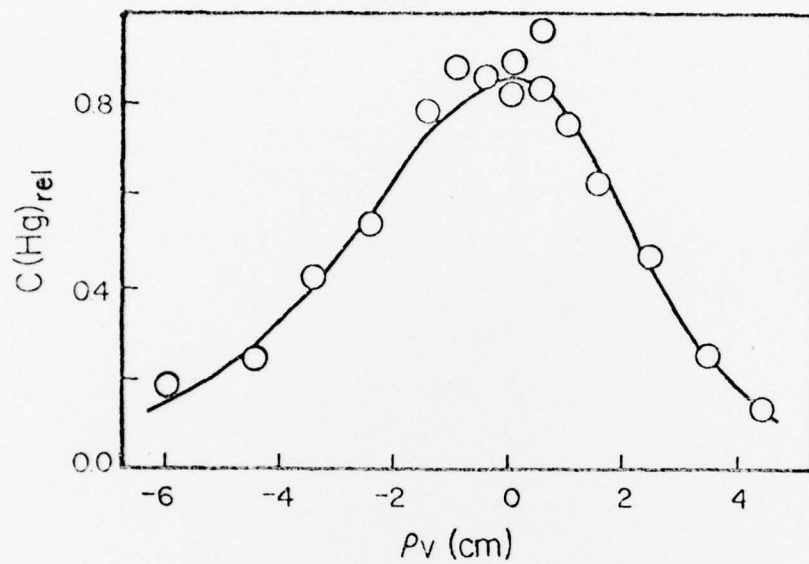
Fig. 10 Calculated transverse concentration profiles in linearized form based on steady-state concentrations determined from Monte Carlo simulations with an assumed value  $\rho_0 = 10 \text{ cm}$ ,  $z = 3.9 \text{ cm}$ ,  $\lambda = 0.02$ ,  $u(0) = 2.7 \times 10^{-3}$ ,  $P = 3000$ ,  $E_0 = 500$ ,  $U/2D = 2.03 \text{ cm}^{-1}$ ;  $\bigcirc$ , flat profile ( $u(\bar{\rho}) = u(0)$ ). Solid line represents least squares fit (slope =  $\sim 2.07 \text{ cm}^{-1}$ ,  $r^2 > 0.99$ );  $\bullet$ , parabolic profile ( $u(\bar{\rho}) = u(0)(1-\bar{\rho}^2)$ ). Solid line represents least squares fit (slope =  $-1.96 \text{ cm}^{-1}$ ,  $r^2 > 0.99$ );  $\Delta$ , triangular profile ( $u(\bar{\rho}) = u(0)(1-\bar{\rho})$ ). Solid line represents least squares fit (slope =  $\sim 1.72 \text{ cm}^{-1}$ ,  $r^2 > .99$ ). All fits were for data in the range  $0 \leq \bar{\rho} \leq \rho_0/3$  ( $R \approx 5.1 \text{ cm}$ ).

Fig. 11 Comparison of Monte Carlo time development profiles in a flat velocity field with that calculated from eq XXI. Monte Carlo parameters and the physical equivalents ( $\rho_0 = 10 \text{ cm}$ ) are given in the bottom row of Table IV.  $\bigcirc$ ,  $z = 1.9 \text{ cm}$ ,  $\rho = 0.1 \text{ cm}$ ;  $\Delta$ ,  $z = 0.1 \text{ cm}$ ,  $\rho = 1.9 \text{ cm}$ . Solid line calculated for  $R = 1.903 \text{ cm}$ .

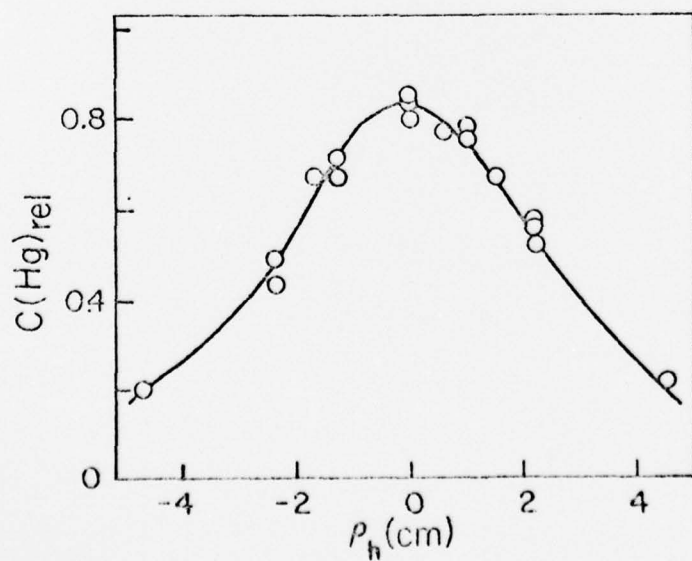
Fig. 12 Comparison of axial Monte Carlo time development profiles with that calculated for flat velocity field by eq XXI (solid curve); the parameters are given in bottom row of Table IV; here  $z = 3.9 \text{ cm}$ ,  $\rho = 0.1 \text{ cm}$ ;  $\bigcirc$ , flat profile ( $u(\bar{\rho}) = u(0)$ );  $\Delta$ , parabolic profile ( $u(\bar{\rho}) = u(0)(1-\bar{\rho}^2)$ ).

Fig. 13 Comparison of off-axis Monte Carlo time development profile with that calculated for flat velocity field by eq XI (solid curve).  $z = \rho = 2.9 \text{ cm}$ . Other parameters are given in bottom row of Table IV.  $\bigcirc$ , flat profile ( $u(\bar{\rho}) = u(0)$ );  $\Delta$ , parabolic profile ( $u(\bar{\rho}) = u(0)(1-\bar{\rho}^2)$ );  $\bullet$ , triangular profile ( $u(\bar{\rho}) = u(0)(1-\bar{\rho})$ ).

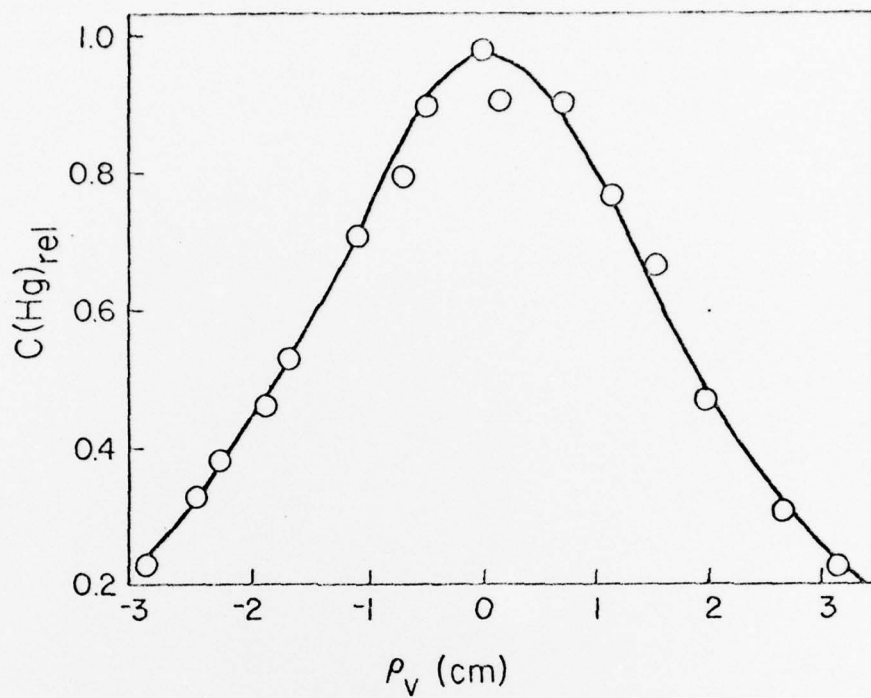




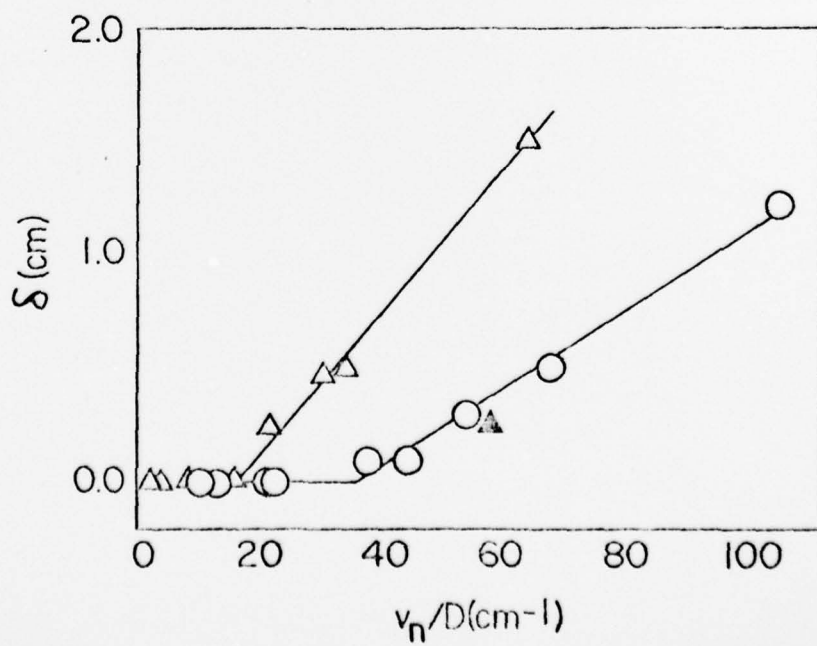
3



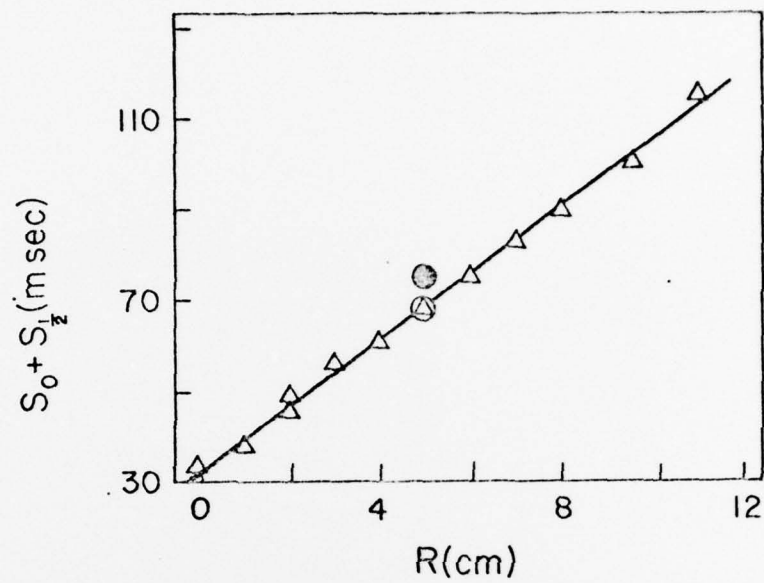
4



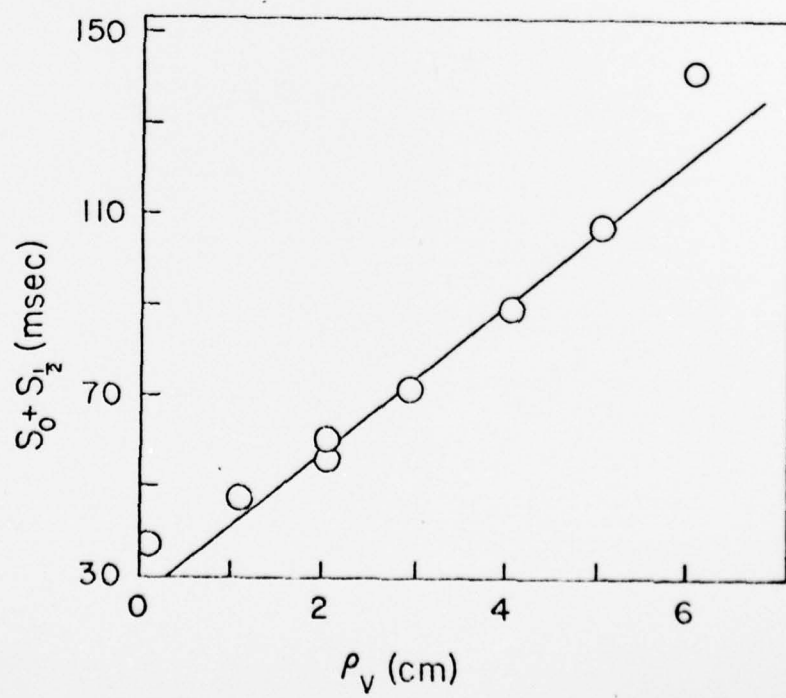
6



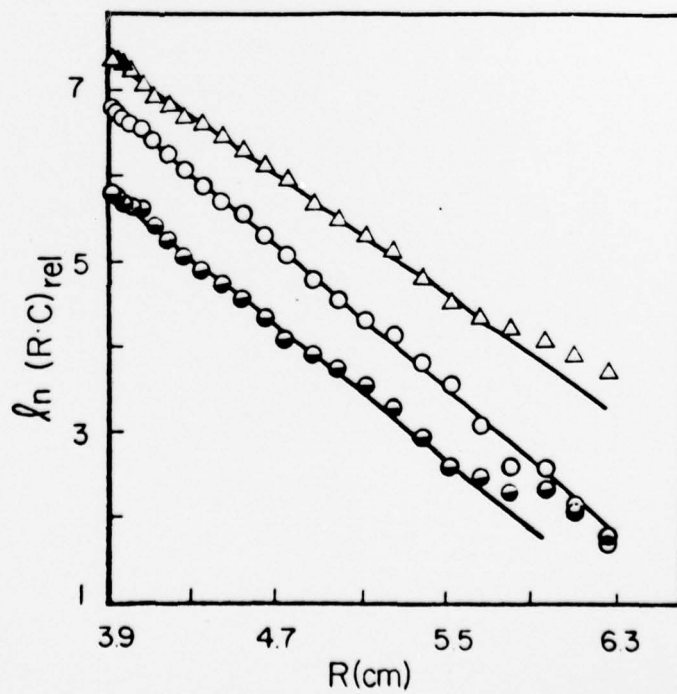
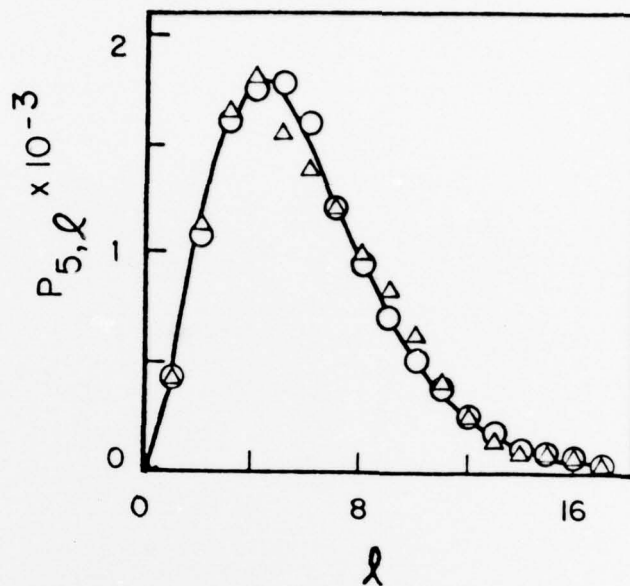
5

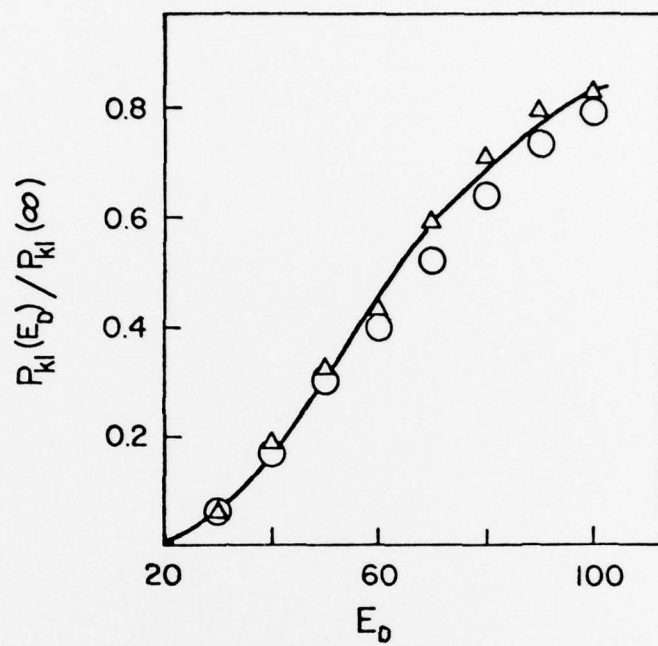


7

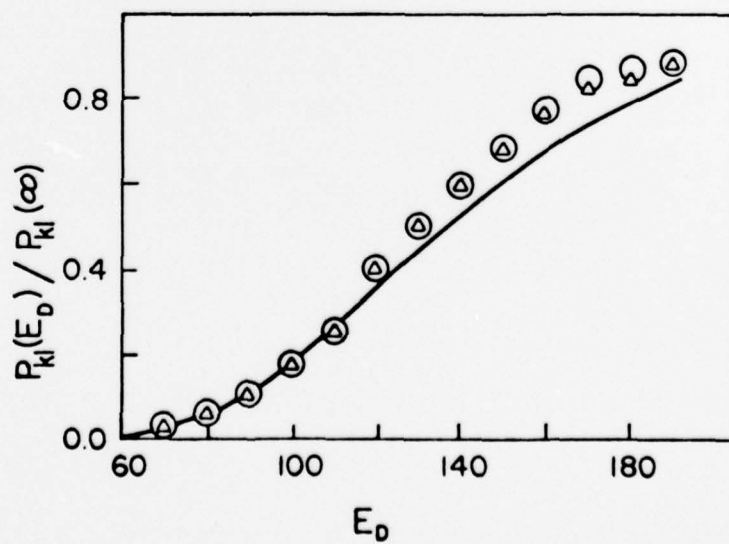


8





//



/2

